Journal of Sound and Vibration 499 (2021) 116000

Contents lists available at ScienceDirect

Journal of Sound and Vibration

journal homepage: www.elsevier.com/locate/jsv

Semi-active vibration control unit tuned to maximise electric power dissipation ☆

Paolo Gardonio[a,*], Emanuele Turco[a], Aleksander Kras[b], Loris Dal Bo[a], Daniel Casagrande[c]

[a] Università degli Studi di Udine, DPIA, Via delle Scienze, 208 - 33100 Udine, Italy
[b] Nanores, Bierutowska 57-59, 51-317 Wrocław, Poland
[c] University of O'Higgins, Avenida Libertador O'Higgins 611, 2820000 Rancagua, Chile

ARTICLE INFO

Article history:
Received 16 December 2020
Revised 30 January 2021
Accepted 1 February 2021
Available online 3 February 2021

Keywords:
Semi-active vibration control
Electromagnetic control unit
On-line tuning
Vibration power absorption
Electric power absorption

ABSTRACT

This paper proposes a local approach for the on-line tuning of a semi-active vibration control unit, which is set to reduce the resonant response of target low-order flexural modes of distributed structures subject to broadband stochastic disturbances. The idea is to have multiple self-contained units, which can be fixed on thin walled structures to reduce flexural vibration and sound radiation at low audio frequencies where the dynamics of the structures is controlled by the resonant response of low-order flexural modes. The unit is formed by an electromagnetic seismic transducer connected to a resistive-inductive shunt. The proposed local tuning criterion is based on the maximisation of the time-averaged electrical power dissipated by the shunt. Both simulation and experimental results are presented for a setup where a unit is mounted on a thin plate model wall-structure excited by a broadband random force and is set to reduce the resonant response of target flexural modes. The paper investigates the physics of four tuning criteria with reference to the resonant response of the target flexural natural modes. First, the minimisation of the time-averaged total flexural kinetic energy of the plate; second, the maximisation of the time-averaged vibration power absorbed by the unit; third, the maximisation of the time-averaged mechanical power dissipated by the transducer and fourth, the maximisation of the time-averaged electrical power dissipated by the coil and shunt. The paper shows that, for small mechanical and Eddy currents damping effects of the transducer, the maximisation of the time-averaged electric power dissipated by the coil and shunt gives similar tuning parameters, and thus comparable vibration control effects, than the reference cost function based on the minimisation of the time-averaged total flexural kinetic energy of the plate.

1. Introduction

This paper investigates the physics of a local approach for the on-line tuning of a vibration control unit formed by an electromagnetic transducer connected to a Resistive-Inductive (RL) shunt. The electromagnetic transducer is composed by

☆ Handling editor: E Chatzi.

* Corresponding author.
E-mail address: paolo.gardonio@uniud.it (P. Gardonio).

https://doi.org/10.1016/j.jsv.2021.116000

an inner permanent magnet, which is fixed to the hosting structure, and an outer ferromagnetic ring with a double coil at its interior, which is held by springs. Therefore the unit works as a seismic device, which generates a control point force on the hosting structure. For conciseness, in the forthcoming part of the paper, the unit will be described as a "seismic electromagnetic transducer connected to a resistive-inductive shunt". The unit is set to attenuate the resonant response of target flexural modes of distributed thin walled structures subject to a broadband stochastic disturbance. The overall objective of the study is to develop a modular unit, which can be used in batches to control the flexural vibration and sound radiation of thin walled structures at low audio frequencies, where the dynamics of the structures is characterised by the resonant responses of low-order flexural modes.

The design of passenger transportation vehicles (aircraft, cars, trains, ships, etc.) increasingly involves new lightweight materials and structures, which, however, are characterised by poor vibration and sound radiation insulation properties [1–3]. Passive treatments, e.g. viscoelastic damping layers, sound insulation linings, stiffeners, mass additions, can be successfully employed to control the vibro-acoustic response of thin wall structures [4,5]. However, the stringent weight requirements set for transportation vehicles, limit the amount of materials that can be used and thus their effectiveness; particularly at low frequencies where the flexural response of the thin wall structures is normally characterised by distinct resonant responses of low order flexural modes [6]. At low frequencies, alternative vibration control approaches should be sought as for example Tuned Vibration Absorbers (TVA) [7], which can be effectively employed to control the resonant response of target low-order modes of distributed structures [8]. These systems normally encompass a seismic mass mounted on a spring-damper element, whose natural frequency and damping ratio are finely tuned with respect to the modal properties, i.e. modal mass and modal stiffness, of the target mode of the hosting structure to be controlled. As discussed in Ref. [9], over the years, several tuning criteria have been proposed for the natural frequency and damping ratio parameters of the TVA, which can be grouped in two principal categories. The first refers to H_∞-like cost functions [7,10], which minimise the peak value of the frequency response of the hosting system. The second considers H_2-like cost functions [8,11], which minimise the integral of the frequency response of the hosting system. In general, both types of cost functions are based on knowledge of the resonant response of the hosting system. When the TVA is mounted on distributed structures to control the resonant response of a specific flexural mode, these cost functions require an estimate of the spatial response of the target flexural mode, which is rather difficult to obtain in practice. Moreover, the dynamic response of wall-structures may vary significantly during vehicle operation (due to tensioning effects or temperature changes) or during vehicle lifetime (due to wearing or physical degradation of materials). Therefore, to successfully track the natural frequency and inherent damping ratio of the target resonant mode the tuning of the TVA should be continuously adapted [12] or swept [13].

Recently, Zilletti *et al.* [9], proposed a local H_2 cost function, which is based on the vibration power absorbed by the TVA. They have shown that, for a simple mass-spring-damper hosting system, this local tuning criterion would provide the same tuning laws as the classical H_2 criterion based on the minimisation of the total flexural kinetic energy of the hosting system. A similar approach was employed also by Camperi *et al.* [14] to tune the feedback gain of a fully active modular vibration control unit encompassing a seismic electromagnetic point force actuator. Overall, this is a very appealing solution since the vibration power cost function can be measured locally at the footprint of the TVA without knowledge of the overall vibration field of the structure. In this way an adaptive TVA can be developed, which continuously updates its fundamental natural frequency and damping ratio to maximise the mechanical power absorption and thus to minimise the overall response of the hosting system, even in presence of large variations of the structure dynamic response. However, to have an adaptive TVA, special spring and damping components should be employed, whose physical properties can be suitably varied. A few options have been proposed over the years, which, for example, employed shape memory alloys elements [15–17] or magneto-rheological and electro-rheological fluids [18]. Alternatively, piezoelectric strain transducers [19–21] and electromagnetic seismic transducers [22–26] connected to shunt circuits have also been employed.

In this paper, the local tuning of a semi-active vibration control unit formed exactly by an electromagnetic seismic transducer connected to a shunt circuit is investigated. Both simulation and experimental results are presented for a setup where the shunted electromagnetic seismic transducer is mounted on a thin plate model wall structure excited in bending by a broadband random force and is tuned to reduce the resonant response of a target flexural mode. This model structure suitably represents the typical flexural response of thin walled structures encountered in transportation vehicles [1–3]. In fact, these structures are characterised by a small modal overlap at low frequencies, such that the flexural vibration is controlled by the resonant response of low-order flexural modes, and then an increasingly larger modal overlap at higher frequencies where the flexural vibration is controlled by the overlap of multiple resonant modes [6]. Indeed the thin plate considered in this study is characterised by a modal overlap that rises linearly with frequency [7] such that, at low audio frequencies, its flexural vibration is characterised by well-separated resonant responses of the first few flexural modes.

The study contrasts the physical effects produced by four tuning criteria with reference to the resonant response of a target flexural mode of the hosting plate structure. To start with, the minimisation of the time-averaged total flexural kinetic energy of the plate; second, the maximisation of the time-averaged vibration power absorbed by the unit; third, the maximisation of the time-averaged mechanical power dissipated by the transducer and fourth, the maximisation of the time-averaged electric power dissipated by the coil and shunt. The objective of the study is to investigate the physics of these tuning criteria and to show how, for small intrinsic damping of the electromagnetic seismic transducer, the maximisation of the time-averaged electric power dissipated by the coil and shunt gives equivalent tuning parameters than the reference cost function based on the minimisation of the time-averaged total flexural kinetic energy of the plate. In this case, the shunted electromagnetic vibration absorber can be conveniently tuned to minimise the resonant response of a target mode

of the hosting structure simply by setting the resistance and inductance of the shunt to maximise the time-averaged electric power dissipated by the coil and shunt with reference to the target mode. This is quite an appealing solution, which can be implemented locally in the shunt without the need of sensors and signal conditioning equipment. In this way a rather compact and lightweight self-contained unit can be developed, which can be deployed in batches on thin walled structures to control the low frequency resonant flexural vibration and sound radiation.

The study is organised in three parts. Firstly, Section 2 is focused on the power absorption and power dissipation properties of the unit with respect to the shunt resistance and inductance parameters. Then, Section 3 presents simulation and experimental parametric studies on the optimal tuning of the resistive-inductive components of the shunt when the unit is mounted on the thin plate wall structure to control the resonant response of a target flexural mode. Finally, Section 4 summarises the principal conclusions of the study.

2. Power absorption and dissipation by the unit

This section presents an introductory overview of the power absorption and dissipation properties when the semi-active unit considered in this study is freely suspended and excited by a force-source at the base. The analysis is based on a parametric study with respect to a wide range of shunt resistances and inductances of the following parameters: a) the time-averaged vibration power absorbed to the unit $\bar{P}_a$, b) the time-averaged mechanical power dissipated by the transducer $\bar{P}_m$ and c) the time-averaged electric power dissipated by the coil and shunt components $\bar{P}_e$.

2.1. Shunted electromagnetic transducer response

As shown in Fig. 1(a),(b) the electromagnetic transducer considered in this study is composed by an inner permanent magnet and an outer ferromagnetic ring with a double coil at its interior, which are connected at the bottom and top ends by spiral springs [27]. The coil terminals are connected to a simple shunt circuit formed by a resistor and an inductor connected in series. The physical properties of the transducer are summarised in Table 1.

As discussed in Refs. [24–26], the typical aggregate resistive and aggregate inductive effects of the coil and shunt necessary to minimise the resonant response of a hosting thin panel structure excited in bending may be lower than the intrinsic coil resistance and inductance of the transducer at hand. Therefore, in some cases, the shunt should actually implement a negative inductance and a negative resistance, which partially compensate the coil inductance and resistance respectively. For this reason, the parametric studies presented in this paper refer to negative shunt inductances and resistances too. To avoid the unit goes unstable, the range of negative shunt resistance was carefully chosen in such a way as to guarantee the coil and shunt aggregate resistive effect is positive.

The response of the shunted transducer is modelled with the electro-mechanical lumped parameter model shown in Fig. 1(c). Here the base mass m_b and the seismic mass m_a represent the inertial effects of the inner permanent magnet and

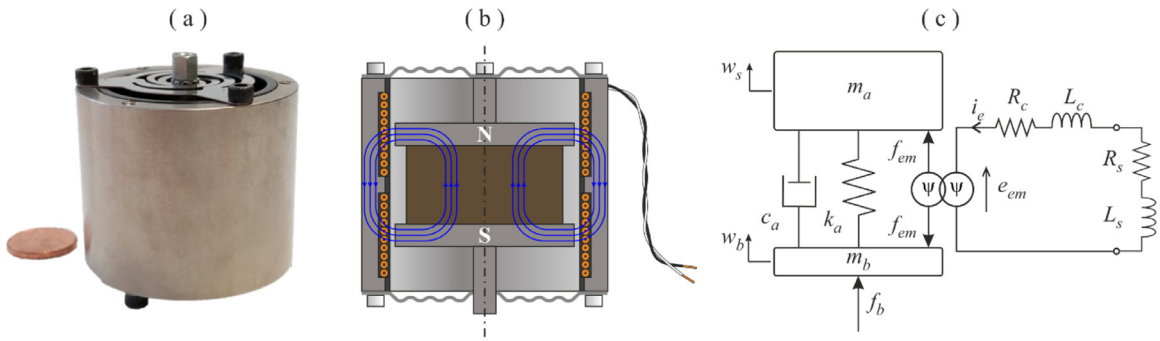

Fig. 1. (a) Picture and (b) sketch of the electromagnetic transducer. (c) Lumped parameter model of the electromagnetic transducer connected to a resistive-inductive shunt.

Table 1
Physical properties of the electromagnetic transducer.

Parameter	Value
Base mass	$m_b = 115$ [g]
Suspended mass	$m_a = 185$ [g]
Fundamental natural frequency	$f_{EM} = 18$ [Hz]
Damping ratio	$\zeta_{EM} = 22$ [%]
Coil resistance	$R_c = 22.5$ [Ω]
Coil inductance	$L_c = 6.25$ [mH]
Transduction coefficient	$\psi = 22.5$ [N/A]

of the external ferromagnetic ring and double coil assembly respectively. Also, the spring k_a gives the total axial stiffness of the spiral springs whereas the damper c_a provides the intrinsic mechanical damping effects due to the losses produced by the Couette air flow in the small gap between the inner permanent magnet and the double coil [28] and by the Eddy currents in the moving ferro-magnetic ring [29,30]. The resistance R_c and inductance L_c provide the resistive and inductive effects of the coil. Therefore, the model doesn't take into account the lossy inductive effect produced by the Eddy currents that develops in the magnetic components, which in fact is negligible in the low frequency range where the shunted transducer actually operates [31,32]. The transduction effects are modelled with the two-port element composed by an ideal current-controlled force generator and an ideal velocity-controlled voltage generator [28]. According to Faraday's law, when the ferromagnetic ring and coil assembly moves with respect to the inner permanent magnet with a relative velocity $\dot{w}_a = \dot{w}_s - \dot{w}_b$, a voltage e_{em} proportional to the relative velocity is induced at the terminal of the coil, such that:

$$e_{em}(t) = \psi \dot{w}_a(t), \tag{1}$$

where $\psi = Bl$ is the electromagnetic coupling coefficient given by the product of the magnetic field B due to the permanent magnet and the length l of the coil winding. In addition, according to Ampère's law, when a current i_e is applied to the coil, a reactive axial force f_{em} is generated between the coil-ferromagnetic ring assembly and the inner permanent magnet, which is given by:

$$f_{em}(t) = \psi i_e(t), \tag{2}$$

where ψ is the same electromagnetic coupling coefficient as that in Eq. (1). Finally, as shown in Fig. 1(c), the shunt is simply composed by a resistor R_s and an inductor L_s connected in series.

The electro-mechanical response of the freely suspended transducer connected to the shunt can be derived by applying Newton's law of motion to the base and seismic masses of the transducer and by applying Kirchhoff's voltage law to the coil-shunt electric network. The equations of motion for the transducer base and seismic masses are thus given by:

$$m_b \ddot{w}_b(t) - c_a \dot{w}_a(t) - k_a w_a(t) + f_{em}(t) = f_b(t), \tag{3}$$

$$m_a \ \ddot{w}_s(t) + c_a \dot{w}_a(t) + k_a w_a(t) - f_{em}(t) = 0 \tag{4}$$

where $w_a = w_s - w_b$ and w_b, w_s are the displacements of the base and seismic masses. In the two equations above m_b, m_a, c_a, k_a are the transducer base and seismic masses, damping coefficient and stiffness coefficients respectively. Also, f_{em} is the reactive force produced by the current i_e flowing in the coil of the transducer given in Eq. (2). Finally $f_b(t)$ is the force exerted on the base mass. The equation for the electric response of the coil and shunt network is given by:

$$e_{em}(t) + (R_c + R_s) i_e + (L_c + L_s) \frac{di_e}{dt} = 0, \tag{5}$$

where $e_{em}(t)$ is the back electro-motive force given in Eq. (1), i_e is the current flow in the coil and shunt electric network and, finally, R_c, L_c and R_s, L_s are the resistance and inductance of the coil and shunt components respectively. Eqs. (3) – (5) are then casted together in the following matrix equation

$$\begin{bmatrix} m_b & 0 & 0 \\ 0 & m_a & 0 \\ 0 & 0 & 0 \end{bmatrix} \begin{Bmatrix} \ddot{w}_b \\ \ddot{w}_s \\ \ddot{i}_e \end{Bmatrix} + \begin{bmatrix} c_a & -c_a & 0 \\ -c_a & c_a & 0 \\ -\psi & \psi & L_c + L_s \end{bmatrix} \begin{Bmatrix} \dot{w}_b \\ \dot{w}_s \\ \dot{i}_e \end{Bmatrix} + \begin{bmatrix} k_a & -k_a & \psi \\ -k_a & k_a & -\psi \\ 0 & 0 & R_c + R_s \end{bmatrix} \begin{Bmatrix} w_b \\ w_s \\ i_e \end{Bmatrix} = \begin{bmatrix} 1 \\ 0 \\ 0 \end{bmatrix} f_b, \tag{6}$$

which, for simplicity, is rewritten in the following compact form,

$$\mathbf{M}_a \ddot{\mathbf{q}}_a(t) + \mathbf{C}_a \dot{\mathbf{q}}_a(t) + \mathbf{K}_a \mathbf{q}_a(t) = \boldsymbol{\eta}_f f_b(t) \tag{7}$$

Here $\mathbf{q}_a(t) = [w_b \quad w_s \quad i_e]^T$, $\boldsymbol{\eta}_f = [1 \quad 0 \quad 0]^T$, where ^{T} is the transpose matrix operator. Also, the mass damping and stiffness matrices M_a, C_a, K_a can be readily derived from Eq. (6). Assuming time-harmonic vibrations, such that the harmonic functions are expressed in the following complex form $f(t) = \mathrm{Re}\{f(\omega)\exp(\mathrm{j}\omega t)\}$, where $f(\omega)$ is the complex amplitude, ω is the circular frequency and $\mathrm{j} = \sqrt{-1}$, Eq. (7) becomes

$$\left(-\omega^2 \mathbf{M}_a + j\omega \mathbf{C}_a + \mathbf{K}_a\right) \mathbf{q}_a(\omega) = \boldsymbol{\eta}_f f_b(\omega) \ . \tag{8}$$

Thus, the vector $\dot{\mathbf{q}}_a(\omega)$ with the complex amplitudes of the vector $\dot{\mathbf{q}}_a(t)$ can be expressed as

$$\dot{\mathbf{q}}_a(\omega) = \mathbf{Y}_a(\omega) \boldsymbol{\eta}_f f_b(\omega), \tag{9}$$

where $\mathbf{Y}_a(\omega) = j\omega(-\omega^2 \mathbf{M}_a + j\omega \mathbf{C}_a + \mathbf{K}_a)^{-1}$. Also, the complex amplitudes of the base velocity, relative velocity, and current can be readily derived from the following relations:

$$\dot{w}_b(\omega) = \boldsymbol{\eta}_b \mathbf{Y}_a(\omega) \boldsymbol{\eta}_f f_b(\omega), \tag{10}$$

$$\dot{w}_a(\omega) = \boldsymbol{\eta}_a \mathbf{Y}_a(\omega) \boldsymbol{\eta}_f f_b(\omega), \tag{11}$$

$$i_e(\omega) = \frac{1}{j\omega}\boldsymbol{\eta}_i \mathbf{Y}_a(\omega)\boldsymbol{\eta}_f f_b(\omega), \tag{12}$$

where $\boldsymbol{\eta}_b = [1 \quad 0 \quad 0]$ $\boldsymbol{\eta}_a = [-1 \quad 1 \quad 0]$, $\boldsymbol{\eta}_i = [0 \quad 0 \quad 1]$. Moreover, from Eq. (10), the complex amplitude of the force at the base of the transducer results given by

$$f_b(\omega) = Z_b(\omega)\dot{w}_b(\omega), \tag{13}$$

where $Z_b(\omega) = [\boldsymbol{\eta}_b \mathbf{Y}_a(\omega)\boldsymbol{\eta}_f]^{-1}$ is the base impedance of the transducer connected to the shunt. Also, recalling the voltage drop across the coil and shunt elements is given by

$$v_e(t) = (R_c + R_s)i_e(t) + (L_c + L_s)\frac{d}{dt}i_e(t), \tag{14}$$

the complex amplitude of the voltage drop across the coil and shunt results given by

$$v_e(\omega) = Z_e(\omega)i_e(\omega), \tag{15}$$

where $Z_e(\omega) = j\omega(L_e + L_s) + (R_e + R_s)$ is the electric impedance of the coil and shunt components. Finally, the reactive force produced by the mechanical dissipative effects of the transducer is given by

$$f_c(t) = c_a\dot{w}_a(t), \tag{16}$$

such that

$$f_c(\omega) = c_a\dot{w}_a(\omega), \tag{17}$$

where $f_c(\omega)$, $\dot{w}_a(\omega)$ are the complex amplitudes of $f_c(t)$, $\dot{w}_a(t)$ respectively.

2.2. Power functions

As anticipated above, three time-averaged power functions are investigated in this section, which are: a) the time-averaged vibration power absorbed by the unit, $\bar{P}_a$, b) the time-averaged mechanical power dissipated by the transducer, $\bar{P}_m$, c) the time-averaged electrical power dissipated by the coil and shunt components, $\bar{P}_e$. As shown in Ref. [33], these time-averages are actually derived with a frequency domain formulation based on the Power Spectral Densities (PSD) of the power functions [34]:

$$\bar{P}_a = E[f_b(t)\dot{w}_b(t)] = \frac{1}{\pi}\int_0^\infty S_a(\omega)\mathrm{d}\omega, \tag{18}$$

$$\bar{P}_m = E[f_c(t)\dot{w}_a(t)] = \frac{1}{\pi}\int_0^\infty S_m(\omega)\mathrm{d}\omega, \tag{19}$$

$$\bar{P}_e = E[v_e(t)i_e(t)] = \frac{1}{\pi}\int_0^\infty S_e(\omega)\mathrm{d}\omega. \tag{20}$$

Here, $E[]$ is the expectation operator and the PSD of a) the vibration power absorbed by the unit, $S_a(\omega)$, b) the mechanical power dissipated by the transducer, $S_m(\omega)$, and c) the electric power dissipated by the coil and shunt, $S_e(\omega)$, are given by [34]:

$$S_a(\omega) = \lim_{T\to\infty} E\left[\frac{1}{T}\mathrm{Re}\left\{f_b^*(\omega)\dot{w}_b(\omega)\right\}\right], \tag{21}$$

$$S_m(\omega) = \lim_{T\to\infty} E\left[\frac{1}{T}\mathrm{Re}\{f_c^*(\omega)\dot{w}_a(\omega)\}\right], \tag{22}$$

$$S_e(\omega) = \lim_{T\to\infty} E\left[\frac{1}{T}\mathrm{Re}\{v_e^*(\omega)i_e(\omega)\}\right]. \tag{23}$$

In these expressions, * is the complex conjugate operator and $\mathrm{Re}\{\cdot\}$ is the real part operator. Recalling Eqs. (10) – (13), (15), (17) the above PSD expressions become:

$$S_a(\omega) = \lim_{T\to\infty} E\left[\frac{1}{T}\mathrm{Re}\left\{f_b^*(\omega)\frac{1}{Z_b(\omega)}f_b(\omega)\right\}\right] = \frac{1}{\mathrm{Re}\{Z_b(\omega)\}}S_{ff}(\omega), \tag{24}$$

$$S_m(\omega) = \lim_{T\to\infty} E\left[\frac{1}{T}\mathrm{Re}\left\{f_b^*(\omega)\boldsymbol{\eta}_f^{\mathrm{T}}\mathbf{Y}_a^{\mathrm{H}}(\omega)\boldsymbol{\eta}_a^{\mathrm{T}}c_a\boldsymbol{\eta}_a\mathbf{Y}_a(\omega)\boldsymbol{\eta}_f f_b(\omega)\right\}\right] = c_a\boldsymbol{\eta}_f^{\mathrm{T}}\mathbf{Y}_a^{\mathrm{H}}(\omega)\mathbf{T}_a\mathbf{Y}_a(\omega)\boldsymbol{\eta}_f S_{ff}(\omega), \tag{25}$$

$$S_e(\omega) = \frac{1}{\omega^2}\lim_{T\to\infty} E\left[\frac{1}{T}\mathrm{Re}\left\{f_b^*(\omega)\boldsymbol{\eta}_f^{\mathrm{T}}\mathbf{Y}_a^{\mathrm{H}}(\omega)\boldsymbol{\eta}_i^{\mathrm{T}}Z_e^*(\omega)\boldsymbol{\eta}_i\mathbf{Y}_a(\omega)\boldsymbol{\eta}_f f_b(\omega)\right\}\right] = \frac{(R_e + R_s)}{\omega^2}\ \boldsymbol{\eta}_f^{\mathrm{T}}\mathbf{Y}_a^{\mathrm{H}}(\omega)\mathbf{T}_i\mathbf{Y}_a(\omega)\boldsymbol{\eta}_f S_{ff}(\omega), \tag{26}$$

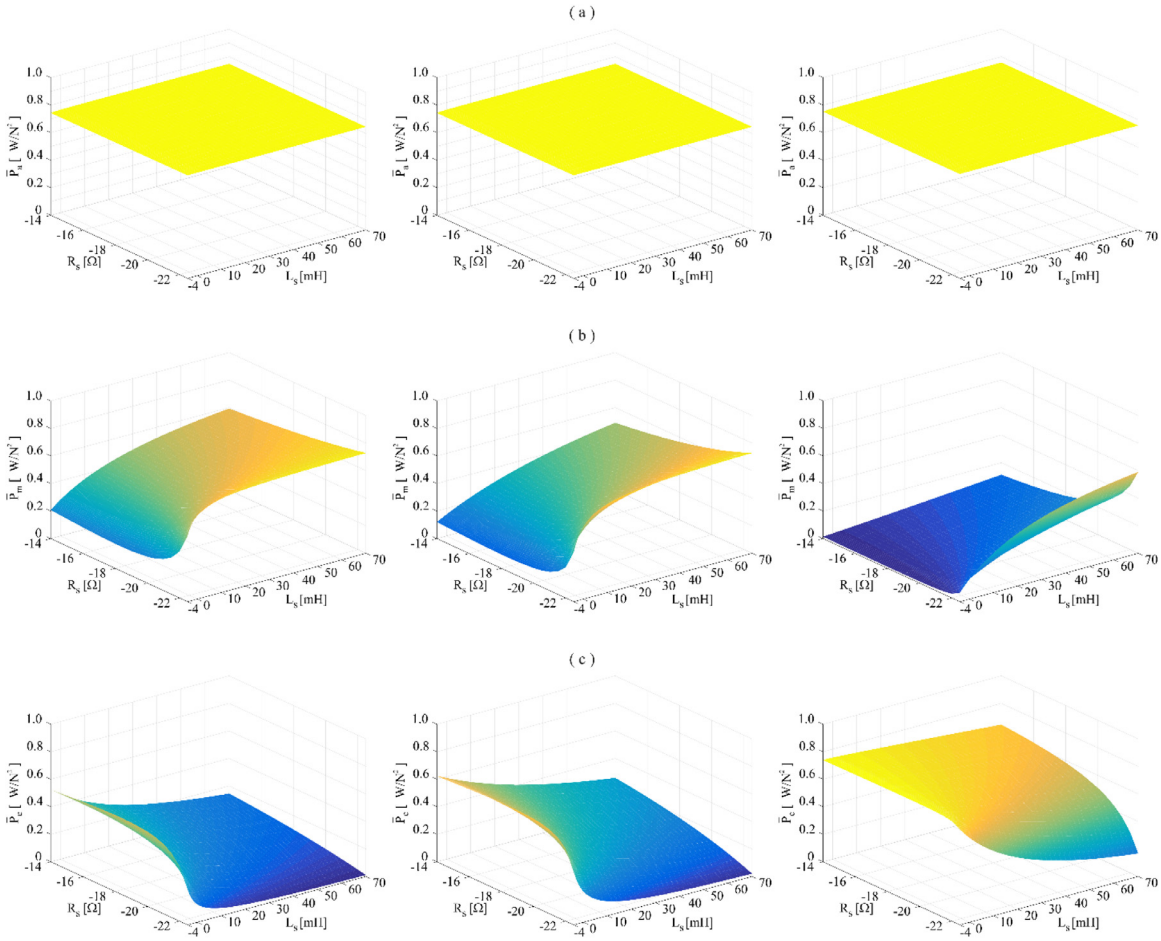

Fig. 2. Time-averaged power functions with respect to the shunt resistance and inductance for inherent mechanical damping ratio $\zeta_{EM} = 22$ %, first column, $\zeta_{EM} = 4$ %, second column, and $\zeta_{EM} = 2$%, third column. (a) power absorbed by the unit, (b) mechanical power dissipated by the transducer, (c) electrical power dissipated by the coil and shunt.

where $\mathbf{T}_a = \boldsymbol{\eta}_a^{\mathrm{T}}\boldsymbol{\eta}_a$, $\mathbf{T}_i = \boldsymbol{\eta}_i^{\mathrm{T}}\boldsymbol{\eta}_i$ and ^{H} is the Hermitian transpose matrix operator. Also,

$$S_{ff}(\omega) = \lim_{T\to\infty} E\left[\frac{1}{T} f_b(\omega) f_b^*(\omega)\right] \equiv 1 \tag{27}$$

is the PSD of the force applied at the base of the transducer, which is assumed to be equal to 1. As discussed above, the damping factor c_a encompasses both the losses produced by the Couette air flow in the small gap between the magnet and the double coil and by the Eddy currents that develop in the moving ferro-magnetic ring. Therefore, both losses depend on the motion between the inner magnet and the outer coil and ferro-magnetic ring assembly. For this reason, the power dissipated by the transducer is referred to as mechanical power.

2.3. Parametric analysis

Fig. 2 shows RL-maps for the three time-averaged power functions listed above, which are depicted by row considering three levels of mechanical damping in the transducer: first column $\zeta_{EM} = 22$ %, second column $\zeta_{EM} = 4$ %, third column $\zeta_{EM} = 2$ %. The first row of plots shows that, for the given ideal force source applied at the base of the free transducer, the time-averaged power absorbed by the unit does not change, neither with the shunt RL components nor with the mechanical damping of the transducer. The study presented in Ref. [26] showed that the shunted electromagnetic transducer considered in this paper can be modelled into an equivalent mass-spring-damper mechanical system, with stiffness and damping effects proportional to both the mechanical stiffness-damping effects of the transducer and to the electrical inductive-resistive effects of the shunt, weighted by the transduction coefficient. In this respect, Refs. [35–39] showed that, the time-averaged power input to, and dissipated by, a mass-spring-damper system exposed to a base stationary white noise acceleration with PSD S_0 is bound to be constant and equal to $P(\omega) = \frac{1}{2}\pi m_a S_0$ [37]. Therefore, it solely depends on the seismic mass of the transducer and the amplitude of the excitation, which confirms the result shown in the first row of plots of Fig. 2.

The second row of the plots in Fig. 2, indicates that the time-averaged mechanical power dissipated by the transducer is greater for large negative shunt resistances, which compensate the inherent resistance of the coil, and for large shunt inductances. Therefore, overall, it is greater for small aggregate coil and shunt resistances. Alternatively, it is lower for small negative shunt resistances, that is for large aggregate coil and resistances, and for small shunt inductances. Contrasting the three plots, it can be noticed that, for given shunt resistance and inductance values, as one would expect, the time averaged mechanical power dissipated by the transducer tends to increase as the transducer damping ratio ζ_{EM} increases.

The third row of plots in Fig. 2, shows that the time-averaged electrical power dissipated by the coil and shunt show matching maps than those found for the time-averaged mechanical power dissipated in the transducer. Thus, the time-averaged electrical power dissipated by the shunt is greater for small negative shunt resistances, that is for large aggregate coil and resistances, and for small shunt inductances. Comparing the three plots, it is also noticed that, for given shunt resistance and inductance values, the time averaged electric power dissipated by the coil and shunt tends to decrease as the transducer damping ratio ζ_{EM} increases.

For completeness, it was verified that, for all resistance and inductance values, the sum of the time-averaged mechanical power dissipated by the transducer (2nd row maps) and time-averaged electrical power dissipated by the coil and shunt (3rd row maps) gives the constant-value time-averaged mechanical power absorbed by the unit (1st row maps).

3. Plate and semi-active control unit

This section investigates the tuning of the semi-active unit to reduce the resonant response of target flexural modes of a thin rectangular plate model structure. This setup satisfies two concurrent requirements. On the one hand, the “simple” geometry of the plate allows a direct comparison of simulation results obtained from analytical formulations with experimental measurements. On the other hand, despite its “simple” geometry, the plate is characterised by the typical low/mid/high-frequencies flexural response features of real structures [6]. In particular, it presents the distinctive low-frequency vibration features characterised by the resonant responses of distinct low-order flexural modes, which is of primary interest for this study.

The effects produced by the following four tuning criteria are examined with reference to the resonant response of a target flexural mode of the plate. The four criteria are based on energy and power cost functions, which are: first, the minimisation of the time-averaged total flexural kinetic energy of the plate; second, the maximisation of the time-averaged vibration power absorbed by the unit; third, the maximisation of the time-averaged mechanical power dissipated by the transducer and fourth, the maximisation of the time-averaged electric power dissipated by the coil and shunt components. Both simulation and experimental results are presented for a setup where the shunted electromagnetic seismic transducer is mounted on a thin plate excited by a broadband random force.

3.1. Hosting structure and semi-active control unit

Fig. 3 shows a scheme and a picture of the arrangement considered in this study, which is composed by a thin rectangular plate made of steel fixed on a rigid frame along the borders. The plate is excited in bending by a point force exerted with a shaker. The flexural response of the plate is measured with a scanner laser vibrometer. Also, the transverse force exerted by the shaker is measured with a load cell. The electromagnetic transducer shown in Fig. 1(a) is fixed to the plate via an impedance head, which gives the force and velocity at the base of the transducer necessary to estimate the vibration

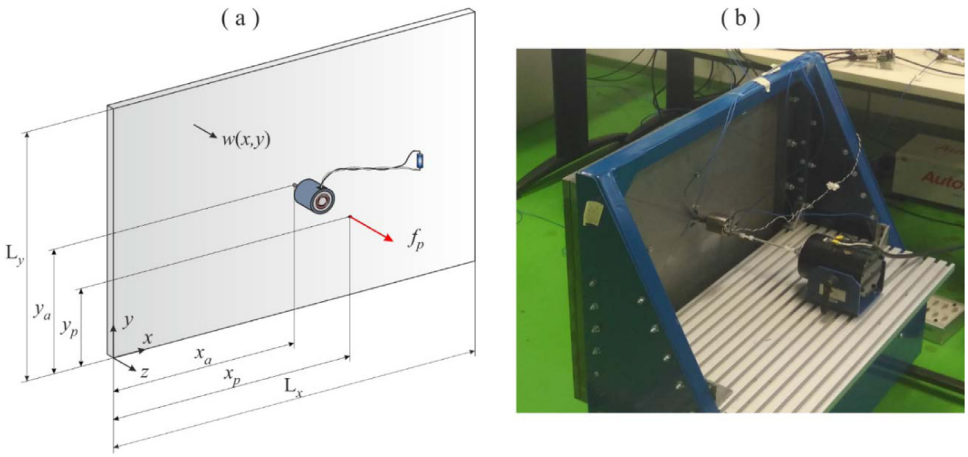

Fig. 3. Thin rectangular plate excited by a stochastic point force, which is equipped with a shunted electromagnetic vibration absorber: (a) sketch; (b) picture of the experimental test rig.

Table 2
Geometrical and physical properties of the rectangular plate.

Parameter	Value
Length	$L_X = 668$ [mm]
Width	$L_y = 444$ [mm]
Thickness	$h = 1.37$ [mm]
Density	$\rho = 8200$ [kg/m^3]
Young's modulus of elasticity	$E = 210 \times 10^9$ [N/m^2]
Poisson ratio	$\nu = 0.31$ [kg/m^3]
Modal damping ratio	$\zeta = 0.1$ [%]
Excitation position	$x_p = 434$ mm, $y_p = 139$ mm
Control position mode 1	$x_{c1} = 334$ mm, $y_{c1} = 222$ mm
Control position mode 2	$x_{c2} = 334$ mm, $y_{c2} = 333$ mm

power absorbed by the unit. The terminals of the transducer coil are connected to a digital board via an interface circuit specifically designed to synthesise digitally the electrical impedance of the shunt circuit. The details of the setup can be found in Ref. [26]. Also, the physical and geometrical parameters of the rectangular plate are summarised in Table 2. The position of the point force excitation was selected in such a way as the flexural modes of the panel that resonate in the considered frequency range are evenly excited. Also, the position of the shunted electromagnetic transducer was chosen in such a way as to achieve the best coupling with the two target modes considered in this study.

3.2. Mathematical model

The mathematical model developed to study the coupled response of the panel and shunted electromagnetic transducer shown in Fig. 3(b) is based on three differential equations, that is: the two equations of motion for the transducer seismic mass and for the transducer base mass and the electric mesh equation for the circuit formed by the coil and shunt components. The three equations (3) – (5) are thus still valid; although, the equation of motion for the base mass should, in this case, encompass also the force produced by the flexural vibration of the plate at the point where the transducer is connected to the plate. To this end, the flexural response of the plate is derived starting from the wave equation for flexural vibrations in thin plates, which according to Refs. [40] is given by:

$$D\nabla^4 w(\mathbf{x},t) + \rho h \ddot{w}(\mathbf{x},t) = f(\mathbf{x},t). \tag{28}$$

Here $w(\mathbf{x},t)$ and $f(\mathbf{x},t)$ are the transverse displacement and the transverse force per unit surface acting on the plate at position $\mathbf{x} = (x,y)$. Also, ρ is the material density, h is the thickness of the plate and $D = \frac{Eh^3}{12(1-\nu^2)}$ is the bending stiffness, being E and ν the Young's modulus and the Poisson ratio of the material. Finally, $\nabla^2 = \frac{\partial^2}{\partial x^2} + \frac{\partial^2}{\partial y^2}$ is the Laplace operator in Cartesian coordinates. The forcing term $f(\mathbf{x},t)$ is given by the sum of two components: first, the primary point force $f_p(t)\delta(\mathbf{x}-\mathbf{x}_p)$, where $\delta(\cdot)$ is the Dirac delta function and $\mathbf{x}_p = (x_p, y_p)$ is the position where the primary point force is exerted. Second, the localised force per unit surface generated at the absorber footprint $f_b(t)\delta(\mathbf{x}-\mathbf{x}_a)$. The resulting force per unit area exerted on the plate can therefore be expressed as:

$$f(\mathbf{x},t) = f_p(t)\delta(\mathbf{x}-\mathbf{x}_p) + f_b(t)\delta(\mathbf{x}-\mathbf{x}_a). \tag{29}$$

The force produced by the shunted electromagnetic absorber at its footprint can be retrieved from the equation of motion of the base mass, i.e. Eq. (3). Therefore, substituting Eq. (3) into (29) and then the resulting equation into Eq. (28) gives:

$$\rho h \ddot{w}(\mathbf{x},t) + m_b \ddot{w}(\mathbf{x}_a,t) + c_a \dot{w}_a(t) + D\nabla^4 w(\mathbf{x},t) + k_a w_a(t) + f_{em}(t) = f_p(t)\delta(\mathbf{x}-\mathbf{x}_p) \tag{30}$$

Assuming synchronous motion, the flexural displacement of the plate can be expressed as the product of a space-function and a time-function [41], and thus can be approximated with the following finite modal summation:

$$w(\mathbf{x},t) = \sum_{r=1}^{N} \phi_r(\mathbf{x}) b_r(t) = \boldsymbol{\phi}(\mathbf{x})\mathbf{b}(t). \tag{31}$$

In this expression, $\phi_r(\mathbf{x})$ and $b_r(t)$ are the r-th flexural mode shape of the rectangular plate and the r-th modal amplitude, assuming $r = 1, \ldots, N$, being N the number of flexural modes considered in the summation. For simplicity, the modal summation is rearranged in terms of the $1 \times N$ row vector with the flexural mode shapes, $\boldsymbol{\phi}(\mathbf{x})$, and of the $N \times 1$ column vector with the modal amplitudes, $\mathbf{b}(t)$.

As shown in Fig. 4, a preliminary modal analysis of the flexural response of the plate mounted on the rig depicted in Fig. 3(b) showed that the flexural natural modes resemble those of a simply supported thin plate. Therefore, they have been taken equal to [40]:

$$\phi_r(\mathbf{x}) = 2\sin\left(\frac{r_1 \pi x}{L_x}\right)\sin\left(\frac{r_2 \pi y}{L_y}\right), \tag{32}$$

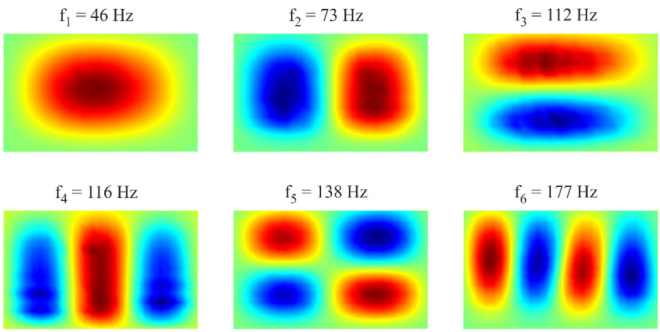

Fig. 4. Measured deflection shapes of the first six flexural modes of the plate with natural frequencies comprised between 10 and 200 Hz.

where $r_1 = 1, 2, \ldots$ and $r_2 = 1, 2, \ldots$ are the modal indices for the r-th mode and L_x and L_y are the lateral dimensions of the plate. However, the preliminary analysis showed that the natural frequencies are instead better described by the formula derived for clamped plates, that is [42]:

$$\omega_r = \pi^2 \sqrt{\frac{D}{\rho h}} \sqrt{\left(\frac{G_x(r_1)}{L_x}\right)^4 + \left(\frac{G_y(r_2)}{L_y}\right)^4 + \frac{2}{(L_x L_y)^2} H_x(r_1) H_y(r_2)}, \tag{33}$$

where for the first flexural natural frequency $G_x(1) = G_y(1) = 1.506$ and $H_x(1) = H_y(1) = 1.248$. Also, for the r-th mode, with modal indices r_1 and r_2, the constants can be obtained with the following expressions: $G_x(r_1) = r_1 + 1/2$, $G_y(r_2) = r_2 + 1/2$, $H_x(r_1) = (r_1 + 1/2)^2(1 - \frac{4}{(2r_1+1)\pi})$ and $H_y(r_2) = (r_2 + 1/2)^2(1 - \frac{4}{(2r_2+1)\pi})$.

At this point, the three differential Eqs. (30), (4) and (5) for the coupled response of the electromagnetic transducer and plate flexural vibrations are rearranged as follows. First, the transducer constitutive Eqs. (1) and (2) are substituted in the three equations. Second, the relative displacement between the base and seismic masses and its derivatives with reference to time are rewritten with respect to the plate transverse displacement at the transducer position, that is:

$$w_a(t) = w_s(t) - w_b(t) = w_s(t) - w(\mathbf{x}_a, t) = w_s(t) - \boldsymbol{\phi}(\mathbf{x}_a)\mathbf{b}(t). \tag{34}$$

Third, the modal summation expression given in Eq. (31) is substituted in $w(\mathbf{x}, t)$ and $w(\mathbf{x}_a, t)$. Fourth, the resulting Eq. (30) is pre-multiplied by the column vector with the flexural mode shapes, $\boldsymbol{\phi}^T(\mathbf{x})$, and integrated over the surface $S = L_x L_y$ of the plate. These mathematical manipulations lead to the following set of $N+2$ equations, which can be written in the following matrix form:

$$\begin{bmatrix} \mathbf{M}_p + \boldsymbol{\phi}^T(\mathbf{x}_a) m_b \boldsymbol{\phi}(\mathbf{x}_a) & \mathbf{0} & \mathbf{0} \\ \mathbf{0} & \mathbf{m}_a & 0 \\ \mathbf{0} & 0 & 0 \end{bmatrix} \begin{Bmatrix} \ddot{\mathbf{b}} \\ \ddot{w}_s \\ \ddot{i}_e \end{Bmatrix} + \begin{bmatrix} \mathbf{C}_p + \boldsymbol{\phi}^T(\mathbf{x}_a) c_a \boldsymbol{\phi}(x_a) & -\boldsymbol{\phi}^T(\mathbf{x}_a) c_a & \mathbf{0} \\ -c_a \boldsymbol{\phi}(\mathbf{x}_a) & c_a & 0 \\ -\psi \boldsymbol{\phi}(\mathbf{x}_a) & \psi & L_c + L_s \end{bmatrix} \begin{Bmatrix} \dot{\mathbf{b}} \\ \dot{w}_s \\ \dot{i}_e \end{Bmatrix}$$

$$+ \begin{bmatrix} \mathbf{K}_p + \boldsymbol{\phi}^T(\mathbf{x}_a) k_a \, \boldsymbol{\phi}(\mathbf{x}_a) & -\boldsymbol{\phi}^T(\mathbf{x}_a) k_a & \boldsymbol{\phi}^T(\mathbf{x}_a) \, \psi \\ -k_a \boldsymbol{\phi}(\mathbf{x}_a) & k_a & -\psi \\ \mathbf{0} & 0 & R_c + R_s \end{bmatrix} \begin{Bmatrix} \mathbf{b} \\ w_s \\ i_e \end{Bmatrix} = \begin{bmatrix} \boldsymbol{\phi}^T(\mathbf{x}_p) \\ 0 \\ 0 \end{bmatrix} f_p \tag{35}$$

Here $\mathbf{M}_p = \rho h \int_S \boldsymbol{\phi}^T(\mathbf{x}) \boldsymbol{\phi}(\mathbf{x}) dS = m_p \mathbf{I}$, $\mathbf{C}_p = 2\zeta \mathbf{M}_p \boldsymbol{\Omega}$ and $\mathbf{K}_p = \mathbf{M}_p \boldsymbol{\Omega}^2$ are the $N \times N$ inertia, damping and stiffness modal matrices of the plate. Also, m_p is the mass of the plate, $\mathbf{I}$ is the $N \times N$ identity matrix, ζ is the modal damping ratio, which is assumed equal for all the modes of the structure. Finally, $\boldsymbol{\Omega}$ is a diagonal matrix whose elements are the plate natural frequencies ω_r, given in Eq. (33). For simplicity, Eq. (35) is written in the following compact form:

$$\mathbf{M}\ddot{\mathbf{q}}(t) + \mathbf{C}\,\dot{\mathbf{q}}\,(t) + \mathbf{K}\mathbf{q}(t) = \boldsymbol{\psi}_f f_p(t), \tag{36}$$

where $\mathbf{q} = [\mathbf{b}^{\mathbf{T}} \quad w_s \quad i_e]^{\mathbf{T}}$, $\boldsymbol{\psi}_f = [\boldsymbol{\phi}(\mathbf{x}_a) \quad 0 \quad 0]^{\mathbf{T}}$ and $\mathbf{M}$, $\mathbf{C}$, $\mathbf{K}$ are the global inertia, damping, stiffness modal matrices of the system, which can be readily derived from Eq. (35).

In this case, assuming time-harmonic vibrations, Eq. (36) becomes

$$\left(-\omega^2 \mathbf{M} + j\omega \mathbf{C} + \mathbf{K}\right)\mathbf{q}(\omega) = \boldsymbol{\psi}_f f_p(\omega), \tag{37}$$

where $\mathbf{q}(\omega)$, $f_p(\omega)$ are the complex amplitudes of $\mathbf{q}(t)$, $f_p(t)$. Hence, as done in Section 2.1, the vector $\dot{\mathbf{q}}(\omega)$ with the complex amplitudes of the velocity terms in the vector $\dot{\mathbf{q}}\,(t)$ is expressed with respect to the modal mobility matrix $\mathbf{Y}(\omega) = j\omega(-\omega^2 \mathbf{M} + j\omega \mathbf{C} + \mathbf{K})^{-1}$, such that:

$$\dot{\mathbf{q}}(\omega) = \mathbf{Y}(\omega) \boldsymbol{\psi}_f f_p(\omega). \tag{38}$$

Also, the complex amplitude of the plate transverse velocity at the generic position $\mathbf{x}$ and at the footprint of the transducer can be derived from the following matrix expressions:

$$\dot{w}(\mathbf{x},\omega) = \boldsymbol{\phi}(\mathbf{x})\dot{\mathbf{b}}(\omega) = \boldsymbol{\psi}(\mathbf{x})\dot{\mathbf{q}}(\omega), \tag{39}$$

$$\dot{w}_b(\omega) = \dot{w}(\mathbf{x}_a,\omega) = \boldsymbol{\phi}(\mathbf{x}_a)\dot{\mathbf{b}}(\omega) = \boldsymbol{\psi}_b\dot{\mathbf{q}}(\omega), \tag{40}$$

where $\boldsymbol{\psi}(\mathbf{x}) = [\boldsymbol{\phi}(\mathbf{x}) \quad 0 \quad 0]$ and $\boldsymbol{\psi}_\mathbf{b} = [\boldsymbol{\phi}(\mathbf{x}_a) \quad 0 \quad 0]$. Moreover, the complex amplitude of the seismic mass velocity can be extracted from Eq. (38) with the following matrix expression

$$\dot{w}_s(\omega) = \boldsymbol{\psi}_s\dot{\mathbf{q}}(\omega) \tag{41}$$

where $\boldsymbol{\psi}_s = [\mathbf{0} \quad 1 \quad 0]$ and $\mathbf{0}$ is a $1 \times N$ vector of zeros. Hence, recalling Eq. (34), the relative velocity between the seismic and base masses, that is the relative velocity between the seismic mass and the transducer footprint position on the plate are given by

$$\dot{w}_a(\omega) = \dot{w}_s(\omega) - \dot{w}_b(\omega) = \boldsymbol{\psi}_a\dot{\mathbf{q}}(\omega) \tag{42}$$

where $\boldsymbol{\psi}_a = [\boldsymbol{\psi}_s - \boldsymbol{\psi}_b]$. Finally, the complex amplitude of the current flowing in the coil and shunt circuit $i_e(\omega)$, can also be extracted from Eq. (38) with the following matrix expression:

$$i_e(\omega) = \frac{1}{j\omega}\boldsymbol{\psi}_i\dot{\mathbf{q}}(\omega) \tag{43}$$

where the vector $\boldsymbol{\psi}_i = [\mathbf{0} \quad 1]$ and 0 is a $1 \times (N+1)$ vector of zeros.

3.3. Tuning laws

As anticipated above, the tuning of the shunt resistive R_s and inductive L_s components is investigated with reference to the following energy and power functions. First, the minimisation of the time-averaged total flexural kinetic energy of the plate $\bar{K}$; second, the maximisation of the time-averaged vibration power absorbed by the unit $\bar{P}_a$; third, the maximisation of the time-averaged mechanical power dissipated by the transducer $\bar{P}_m$ and fourth, the maximisation of the time-averaged electric power dissipated by the coil and shunt components. Recalling the formulation presented in Section 2.2, these time-averaged energy and power functions can be derived with respect to their PSD functions using the following expressions [33,34]:

$$\overline{K}(L_s,R_s) = E\left[\frac{1}{2}\int_S \rho h\dot{w}(\mathbf{x},t)^2 dS\right] = \frac{1}{\pi}\int_{\Delta\omega_r} S_K(\omega)d\omega, \tag{44}$$

$$\overline{P}_a(L_s,R_s) = E[f_b(t)\dot{w}_b(t)] = \frac{1}{\pi}\int_{\Delta\omega_r} S_a(\omega)d\omega, \tag{45}$$

$$\overline{P}_m(L_s,R_s) = E[f_c(t)\dot{w}_a(t)] = \frac{1}{\pi}\int_{\Delta\omega_r} S_m(\omega)d\omega, \tag{46}$$

$$\overline{P}_e(L_s,R_s) = E[v_e(t)i_e(t)] = \frac{1}{\pi}\int_{\Delta\omega_r} S_e(\omega)d\omega. \tag{47}$$

In the above formulae, the bound of integration $\Delta\omega_r = \omega_{r2} - \omega_{r1}$ is centred at the resonance frequency of the r-th target mode, i.e. $\omega_r = \frac{\omega_{r1}+\omega_{r2}}{2}$. The integration frequency band $\Delta\omega$ for the two PSDs functions was selected considering a trade-off between two requirements: firstly, to cover the whole frequency range over which the control unit effectively controls the response of the target resonant mode of the plate and, secondly, to avoid that the device affects only the resonant response of the target mode. The two integration bands for the first and third target modes considered in this study have been marked as $\Delta\omega_1$ and $\Delta\omega_3$ in the forthcoming plots.

As shown in Ref. [33], the PSD of the plate flexural kinetic energy and of the absorbed power and mechanical/electrical dissipated powers in Eqs. (44)–(47) are given by the following relations

$$S_K(\omega) = \frac{1}{2}\rho h\int_S \lim_{T\to\infty} E\left[\frac{1}{T}\ \dot{w}^*(\mathbf{x},\omega)\dot{w}(\mathbf{x},\omega)\right]dS, \tag{48}$$

$$S_a(\omega) = \lim_{T\to\infty} E\left[\frac{1}{T}\mathrm{Re}\left\{f_b^*(\omega)\dot{w}_b(\omega)\right\}\right], \tag{49}$$

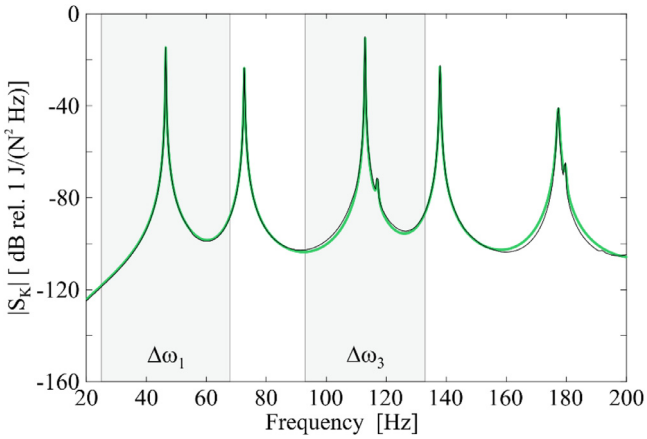

Fig. 5. Simulated (thick green line) and measured (thin black line) flexural kinetic energy PSD per unit PSD of the force excitation of the plain plate.

$$S_m(\omega) = \lim_{T\to\infty} E\left[\frac{1}{T} Re\{f_c^*(\omega)\dot{w}_a(\omega)\}\right], \tag{50}$$

$$S_e(\omega) = \lim_{T\to\infty} E\left[\frac{1}{T} Re\{i_e^*(\omega)v_e(\omega)\}\right]. \tag{51}$$

The PSD of the plate flexural kinetic energy can be suitably derived using Eq. (39) in (48), such that:

$$S_K(\omega) = \frac{1}{2}\rho h \int_S \lim_{T\to\infty} E\left[\frac{1}{T} f_p^*(\omega)\boldsymbol{\psi}_f^T \mathbf{Y}^H(\omega)\boldsymbol{\psi}^T(x)\boldsymbol{\psi}(x)\mathbf{Y}(\omega)\boldsymbol{\psi}_f f_p(\omega)\right] dS = \frac{1}{2} m_p \boldsymbol{\psi}_f^T \mathbf{Y}^H(\omega)\mathbf{H}\mathbf{Y}(\omega)\boldsymbol{\psi}_f S_{ff}(\omega) \tag{52}$$

where $\mathbf{H} = \frac{1}{S}\int_S \boldsymbol{\psi}^T(\mathbf{x})\boldsymbol{\psi}(\mathbf{x})dS$ is a diagonal matrix with the first N-terms equal to 1 and the remaining two terms equal to 0. Also, $S_{ff}(\omega)$ is the PSD of the primary force excitation, which, assuming a white noise process of unit amplitude, is given by [33]:

$$S_{ff}(\omega) = \lim_{T\to\infty} E\left[\frac{1}{T}\ f_p(\omega) f_p^H(\omega)\ \right] \equiv 1. \tag{53}$$

Now, recalling Eqs. (13), (40), the PSD of the power absorbed by the unit given in Eq. (49) results:

$$S_a(\omega) = \lim_{T\to\infty} E\left[\frac{1}{T}\mathrm{Re}\left\{f_p^*(\omega)\boldsymbol{\psi}_f^T\mathbf{Y}^H(\omega)\boldsymbol{\psi}_b^T Z_b^*(\omega)\boldsymbol{\psi}_b\mathbf{Y}(\omega)\boldsymbol{\psi}_f f_p(\omega)\right\}\right] = \mathrm{Re}\left\{Z_b^*(\omega)\right\}\boldsymbol{\psi}_f^T\mathbf{Y}^H(\omega)\mathbf{H}_b\mathbf{Y}(\omega)\boldsymbol{\psi}_f S_{ff}(\omega). \tag{54}$$

Also, recalling Eqs. (17), (42), the PSD of the mechanical power dissipated by the electromagnetic transducer given in Eq. (50) results:

$$S_m(\omega) = \lim_{T\to\infty} E\left[\frac{1}{T}\mathrm{Re}\left\{f_p^*(\omega)\boldsymbol{\psi}_f^T\mathbf{Y}^H(\omega)\boldsymbol{\psi}_a^T c_a\boldsymbol{\psi}_a\mathbf{Y}(\omega)\boldsymbol{\psi}_f f_p(\omega)\right\}\right] = c_a\boldsymbol{\psi}_f^T\mathbf{Y}^H(\omega)\mathbf{H}_a\mathbf{Y}(\omega)\boldsymbol{\psi}_f S_{ff}(\omega). \tag{55}$$

Finally, recalling Eqs. (15), (43), the electrical power dissipated by the coil and shunt components given in Eq. (51) results:

$$S_e(\omega) = \lim_{T\to\infty} E\left[\frac{1}{T}\mathrm{Re}\left\{f_p^*(\omega)\boldsymbol{\psi}_f^T\mathbf{Y}^H(\omega)\boldsymbol{\psi}_i^T\frac{Z_e(\omega)}{\omega^2}\boldsymbol{\psi}_i\mathbf{Y}(\omega)\boldsymbol{\psi}_f f_p(\omega)\right\}\right] = \frac{(R_e+R_s)}{\omega^2}\boldsymbol{\psi}_f^T\mathbf{Y}^H(\omega)\mathbf{H}_i\mathbf{Y}(\omega)\boldsymbol{\psi}_f S_{ff}(\omega). \tag{56}$$

where $\mathbf{H}_b = \boldsymbol{\psi}_b^T\boldsymbol{\psi}_b$, $\mathbf{H}_a = \boldsymbol{\psi}_a^T\boldsymbol{\psi}_a$, $\mathbf{H}_i = \boldsymbol{\psi}_i^T\boldsymbol{\psi}_i$.,

3.4. Experimental validation of the mathematical model

The mathematical model presented above was validated experimentally with the test rig shown in Fig. 3b. More specifically, the simulated PSD of the panel flexural kinetic energy per unit PSD of the force excitation was contrasted with that measured using the laser vibrometer. The spectra in Fig. 5 show a very good agreement between the simulated (thick green line) and the measured (thin black line) PSDs over the entire 20 – 200 Hz frequency range. In particular, the resonance frequencies and the amplitudes of the 7 resonance peaks that characterise the spectra match accurately. This confirms that, as done above, the model should incorporate the flexural natural modes for simply supported plates calculated with Eq. (32) and the natural frequencies for clamped plates derived using Eq. (33). Also, the close overlap of the simulated and measured resonance peaks confirms that the resonant responses of the first eight modes are characterised by a modal damping ratio of 0.1%. The two grey strips in the plot highlight the frequency bands $\Delta\omega_1$ and $\Delta\omega_3$ used to derive the time-averaged energy and power functions given in Eqs. (44) – (47).

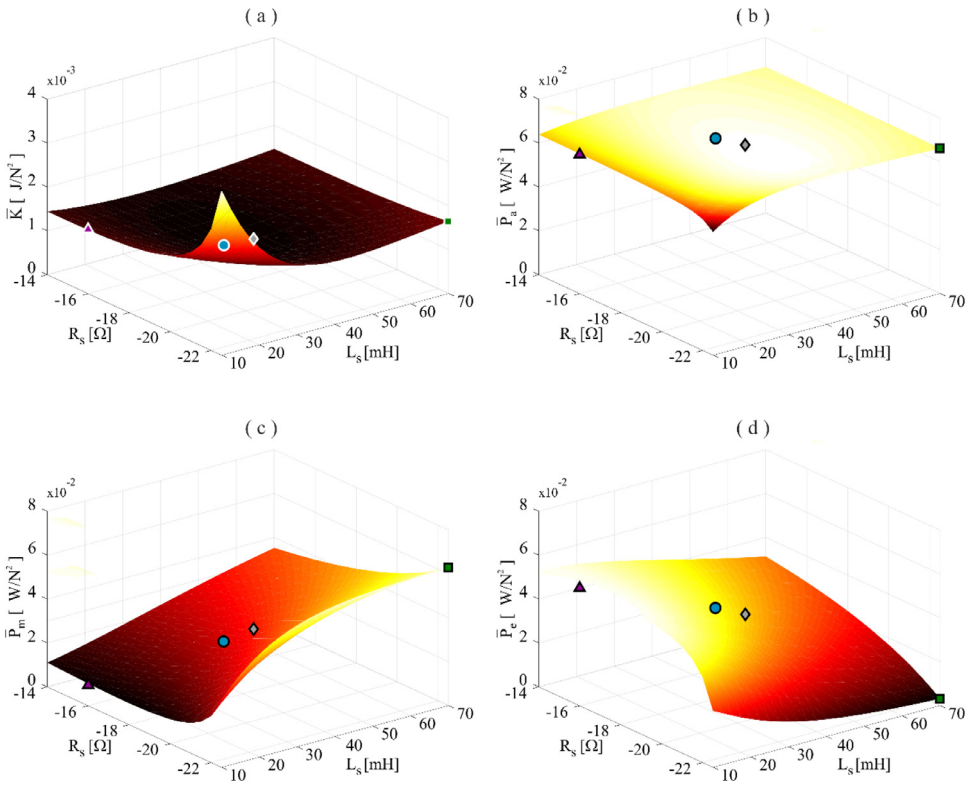

Fig. 6. Simulated time-averaged total flexural kinetic energy of the plate (a), vibration power absorbed by the unit (b), mechanical power dissipated by the transducer (c) and electrical power dissipated by the shunt (d) with respect to the shunt resistance and inductance for the control of the first flexural mode. Cyan circle: minimum of the kinetic energy, grey diamond: maximum of the power absorbed by the unit, green square: maximum of the mechanical power dissipated by the transducer and purple triangle: maximum of the electric power dissipated by the coil and shunt.

4. Tuning analysis

The control effects produced by the shunted electromagnetic absorber on the resonant responses of two flexural modes of the plate are now investigated. More specifically, a parametric study is presented, which shows how the kinetic energy and power functions introduced in Eqs. (44) – (47) vary with reference to the shunt resistance R_s and inductance L_s. The two parameters are selected in ranges such that the shunted electromagnetic absorber can be tuned to control the resonant response of the first and third flexural modes of the plate, which are characterised by natural frequencies at 46 and 112 Hz respectively. More specifically, in the first case, where the device is tuned to control the resonant response of the first flexural mode of the plate, the shunt inductance L_s is varied in the range 10 to 70 mH, which corresponds to variations of the natural frequency of the shunted absorber in the range 62 to 32 Hz. In the second case, where the shunted absorber is tuned to control the resonant response of the third flexural mode of the plate, the shunt inductance L_s is varied in the range -4 to 4 mH, which corresponds to variations of the absorber natural frequency in the range 134 to 78 Hz. In both cases, the shunt resistance R_s is varied in the range -14 to -22.5 Ω.

4.1. Control of the resonant response of the plate first flexural mode

To start with, the tuning of the unit set to control the resonant response of the first flexural mode is investigated. The study considers the four cost functions given in Eqs. (44) – (47) with the frequency integrals derived in the band $\Delta\omega_1$. Figs. 6 and 7 show respectively the simulated and measured maps with respect to the shunt resistance R_s and shunt inductance L_s for the time-averages of: a) the total flexural kinetic energy of the plate, b) the vibration power absorbed by the unit, c) the mechanical power dissipated by the transducer and d) the electrical power dissipated by the coil and shunt. The first row in Tables 3 and 4 summarise the numerical and experimental optimal values of the shunt components for the four energy/power time-averaged functions considered in the simulation and experimental studies respectively.

The simulated maps match reasonably well with the corresponding measured maps. The map (a) with the time-averaged flexural kinetic energy presents an inverse bell-like surface, with a global minimum marked by the cyan circle at $R_s = -18$ Ω and $L_s = 35$ mH. The map (b) with the time-averaged vibration power absorbed by the unit is instead characterised by a flatter bell-like shape with a global maximum marked by the grey diamond, which occurs at $R_s = -19$ Ω and $L_s = 37.5$ mH.

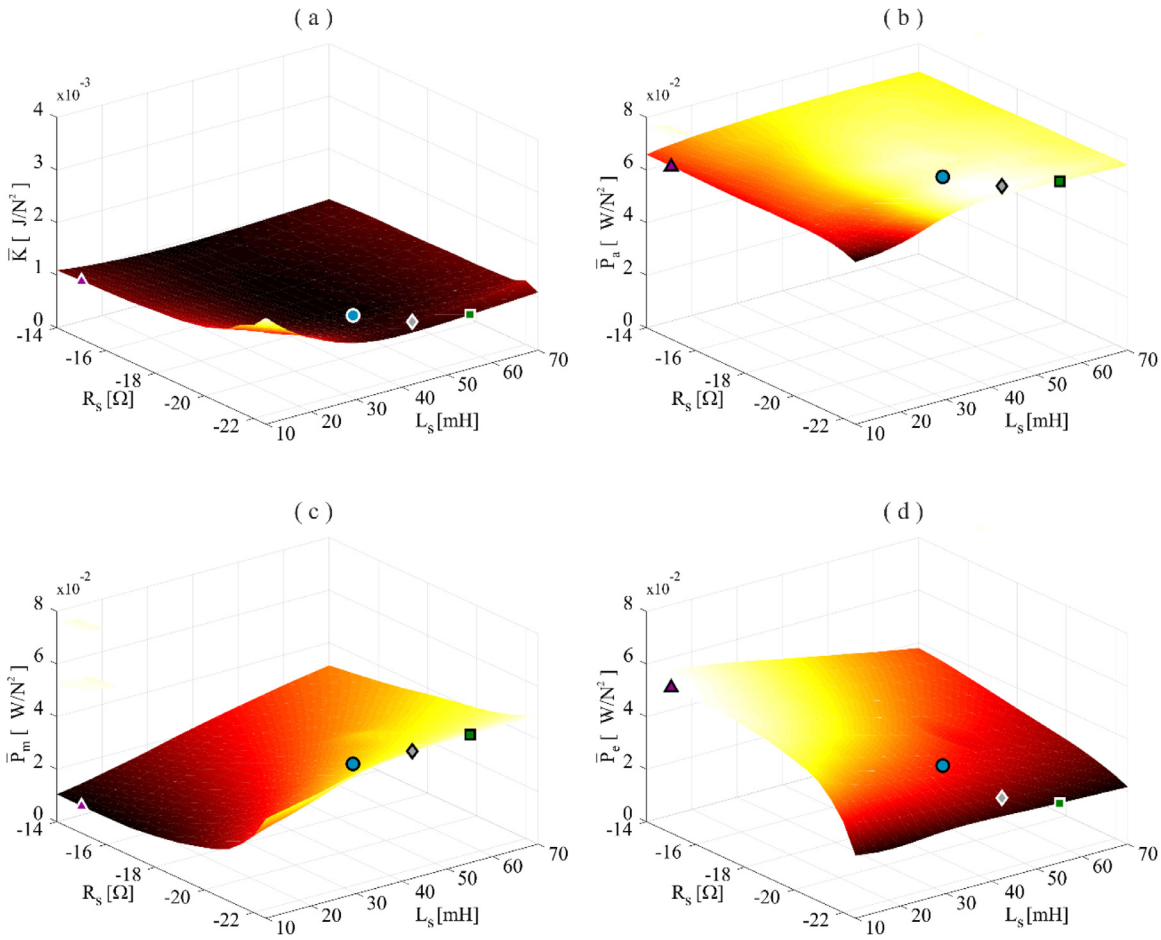

Fig. 7. Measured time-averaged total flexural kinetic energy of the plate (a), vibration power absorbed by the unit (b), mechanical power dissipated by the transducer (c) and electrical power dissipated by the shunt (d) with respect to the shunt resistance and inductance for the control of the first flexural mode. Cyan circle: minimum of the kinetic energy, grey diamond: maximum of the power absorbed by the unit, green square: maximum of the mechanical power dissipated by the transducer and purple triangle: maximum of the electric power dissipated by the coil and shunt.

Table 3
Optimal values of the shunt elements for the minimisation/maximisation of the four energy/power time-averaged functions considered in the simulation study.

Target mode	Natural frequency ω_r[Hz]	Integration bound $\Delta\omega_r$[Hz]	$\arg\min \bar{K}$		$\arg\max \overline{P_a}$		$\arg\max \overline{P_m}$		$\arg\max \overline{P_e}$	
			R_s[Ω]	L_s[mH]	R_s[Ω]	L_s[mH]	R_s[Ω]	L_s[mH]	R_s[Ω]	L_s[mH]
Mode 1	46	40	-18	35	-19	37.5	-22.5	70	-16	10
Mode 3	112	40	-20	-2	-20	-1.5	-22.5	3	-20.5	-1.5

Therefore, as depicted by the cyan circle and grey diamond in the two maps, the minimum of the time-averaged flexural kinetic energy and the maximum of the time-averaged vibration power absorbed by the unit are closely located, although they do not exactly coincide. This little mismatch is likely to be caused by the fact that the integrals in Eqs. (44) and (45) are derived over a finite frequency band $\Delta\omega_1$ for the true response of the hosting structure, which, in this low frequency range, is characterised by the overlap of the resonant responses of the first few flexural modes of the structure [6,8]. Nevertheless, the cyan circle and grey diamond in map (a) indicate that about the same reduction of the time-averaged flexural kinetic energy is produced when the unit is either tuned to minimise the time-averaged flexural kinetic energy itself or to maximise the time-averaged vibration power absorbed by the unit. For the resistance and inductance ranges considered in this study, the maps (c) and (d) with the time-averaged mechanical power dissipated by the transducer and time-averaged electrical power dissipated by the coil and shunt are instead characterised by symmetric quarter sections of bell-like surfaces. Consequently, the time-averaged mechanical power dissipated by the transducer monotonically grows as the shunt inductance increases and the negative shunt resistances becomes larger, that is as the aggregate coil and shunt resistance decreases. Alternatively, the time-averaged electrical power dissipated by the coil and shunt monotonically grows as the

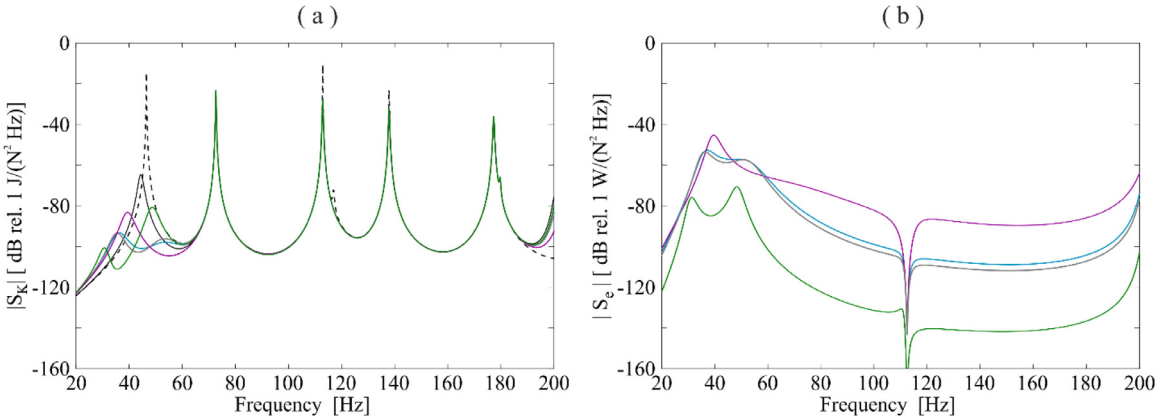

Fig. 8. Simulated spectra of the kinetic energy (a) and electrical power dissipated (b) PSDs for the plain plate (dashed black line) and the plate equipped with the unit in open circuit (solid thin black line) and shunted with optimal values for the minimisation of the time-averaged flexural kinetic energy (cyan lines) and the maximisation of the: time-averaged vibration power absorbed by the unit (grey lines), time-averaged mechanical power dissipated by the transducer (green lines) and time-averaged electrical power dissipated by the coil and shunt (purple lines) when the unit is tuned to control the resonant response of the first flexural mode.

shunt inductance decreases and the negative shunt resistance becomes smaller, that is as the aggregate coil and shunt resistance increases. As seen in Section 2.3 for the freely suspended control unit, the two parameters show complementary variations with respect to the shunt resistance and inductance. Moreover, as highlighted by the green square in map (c), the maximum of the time-averaged mechanical power dissipated by the transducer occurs for the comparatively larger negative shunt resistance $R_s = -22.5\ \Omega$ and shunt inductance $L_s = 70$ mH than the optimal shunt inductance and resistance that either minimise the time-averaged flexural kinetic energy or maximise the time-averaged vibration power absorbed by the unit. Also, according to the purple triangle in map (d), the maximum of the time-averaged electrical power dissipated by the coil and shunt resistance occurs for a comparatively smaller negative shunt resistance $R_s = -16\ \Omega$ and smaller shunt inductance $L_s = 10$ mH than the shunt inductance and resistance that minimise the time-averaged flexural kinetic energy and maximise the time-averaged vibration power absorbed by the unit. Overall, these results suggest that, the time-averaged vibration power absorbed by the unit can be satisfactorily used to tune the shunt inductance and resistance in such a way as the unit minimises the time-average total flexural kinetic energy of the hosting plate.

Indeed, the cyan and grey lines in Figs. 8(a) and 9(a) show that the spectrum of the time-average total flexural kinetic energy is equally reduced at the first resonance frequency when the resistance and inductance of the unit are set to either minimise the time-average total flexural kinetic energy of the plate or to maximise the time-averaged vibration power absorbed by the unit. Instead, the green and purple lines in the two plots indicate that, when the resistance and inductance of the unit are tuned to maximise the time-averaged mechanical power dissipated by the transducer or the time-averaged electric power dissipated by the coil and shunt components, the control effects produced at the first resonance frequency are lower. All this reflects in the simulated and measured spectra of the electric power dissipated by the shunt shown in Figs. 8(b) and 9(b), which, at the first resonance frequency, are comparatively larger when the shunt resistance and inductance are set to either minimise the time-averaged flexural kinetic energy or to maximise the time-averaged vibration power absorbed by the unit.

4.2. Control of the resonant response of the plate third flexural mode

The tuning of the semi-active vibration control unit set to control the resonant response of the third flexural mode is now investigated. In this case, the four cost functions are derived numerically and experimentally with the frequency integrals in Eqs. (44) – (47) calculated in the frequency range $\Delta\omega_3$. Figs. 10 and 11 show the same simulated and measured maps as Figs. 6 and 7. Also, Figs. 12 and 13 show the same simulated and measured spectra as Figs. 8 and 9. The second row in Tables 4 and 5 summarise the numerical and experimental optimal values of the shunt components for the four energy/power time-averaged functions considered in the simulation and experimental studies. Yet again, the simulated maps and spectra match reasonably well the corresponding measured maps and spectra. The cyan circle and grey diamond in the maps (a) and (b) indicate that the minimum and maximum of the time-averaged flexural kinetic energy and time-averaged vibration power absorbed by the unit are now quite close to each other. Indeed, the time-averaged flexural kinetic energy is minimised when $R_s = -20\ \Omega$ and $L_s = -2$ mH whereas the time-averaged vibration power absorbed by the unit is maximised when $R_s = -20\ \Omega$ and $L_s = -1.5$ mH. More importantly, the cyan circle and grey diamond in map (a) clearly show that the reductions of the time-averaged flexural kinetic energy produced when either shunt parameters are implemented closely coincide. This further confirms that the semi-active control unit can be conveniently tuned by maximising the time-averaged vibration power it absorbs. The maps (c) and (d) with the time-averaged mechanical power dissipated by

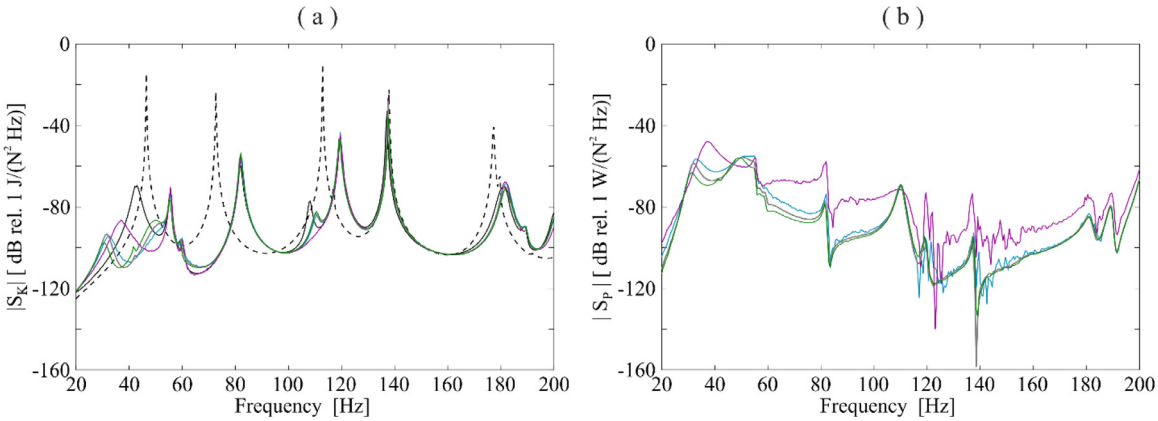

Fig. 9. Measured spectra of the kinetic energy (a) and electrical power dissipated (b) PSDs for the plain plate (dashed black line) and the plate equipped with the unit in open circuit (solid thin black line) and shunted with optimal values for the minimisation of the time-averaged flexural kinetic energy (cyan lines) and the maximisation of the: time-averaged vibration power absorbed by the unit (grey lines), time-averaged mechanical power dissipated by the transducer (green lines) and time-averaged electrical power dissipated by the coil and shunt (purple lines) when the unit is tuned to control the resonant response of the first flexural mode.

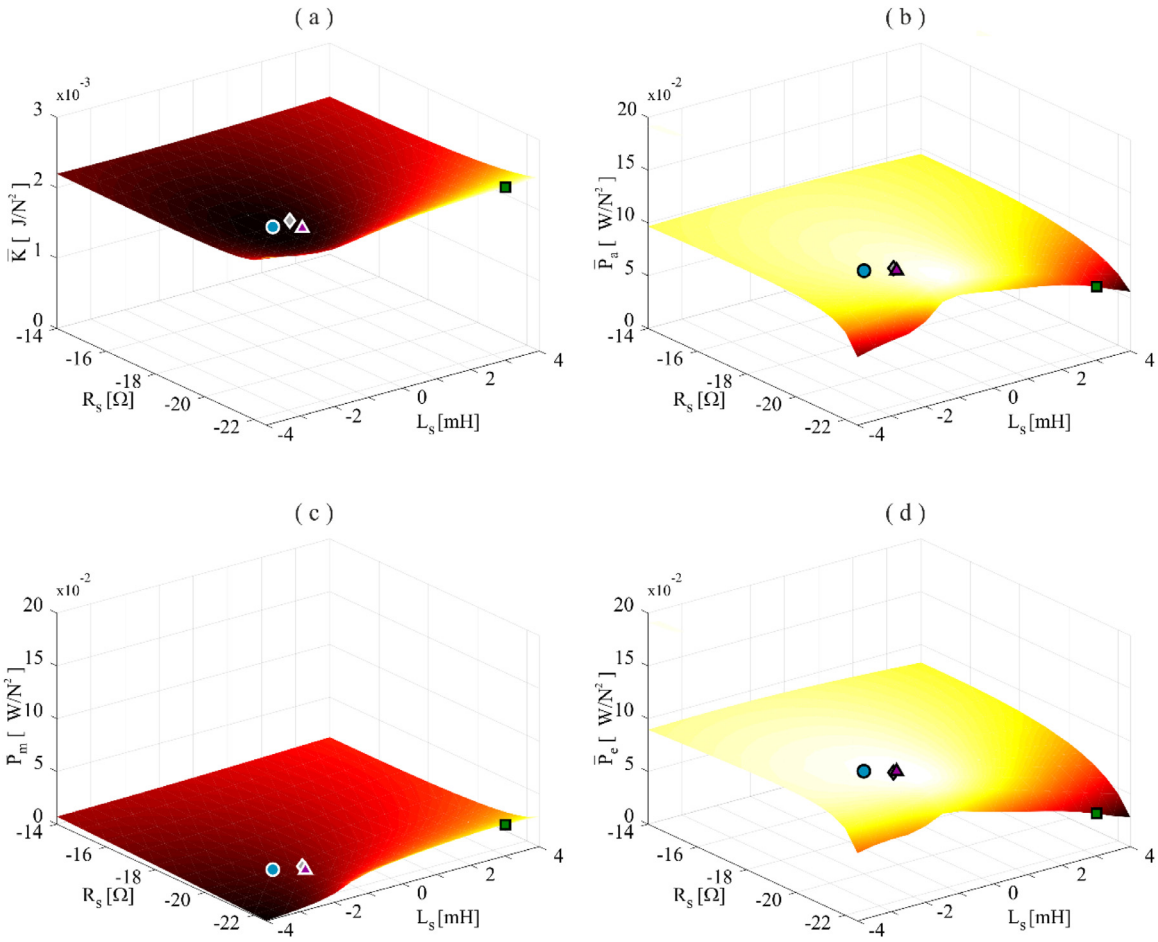

Fig. 10. Simulated time-averaged total flexural kinetic energy of the plate (a), vibration power absorbed by the unit (b), mechanical power dissipated by the transducer (c) and electrical power dissipated by the shunt (d) with respect to the shunt resistance and inductance for the control of the third flexural mode. Cyan circle: minimum of the kinetic energy, grey diamond: maximum of the power absorbed by the unit, green square: maximum of the mechanical power dissipated by the transducer and purple triangle: maximum of the electric power dissipated by the coil and shunt.

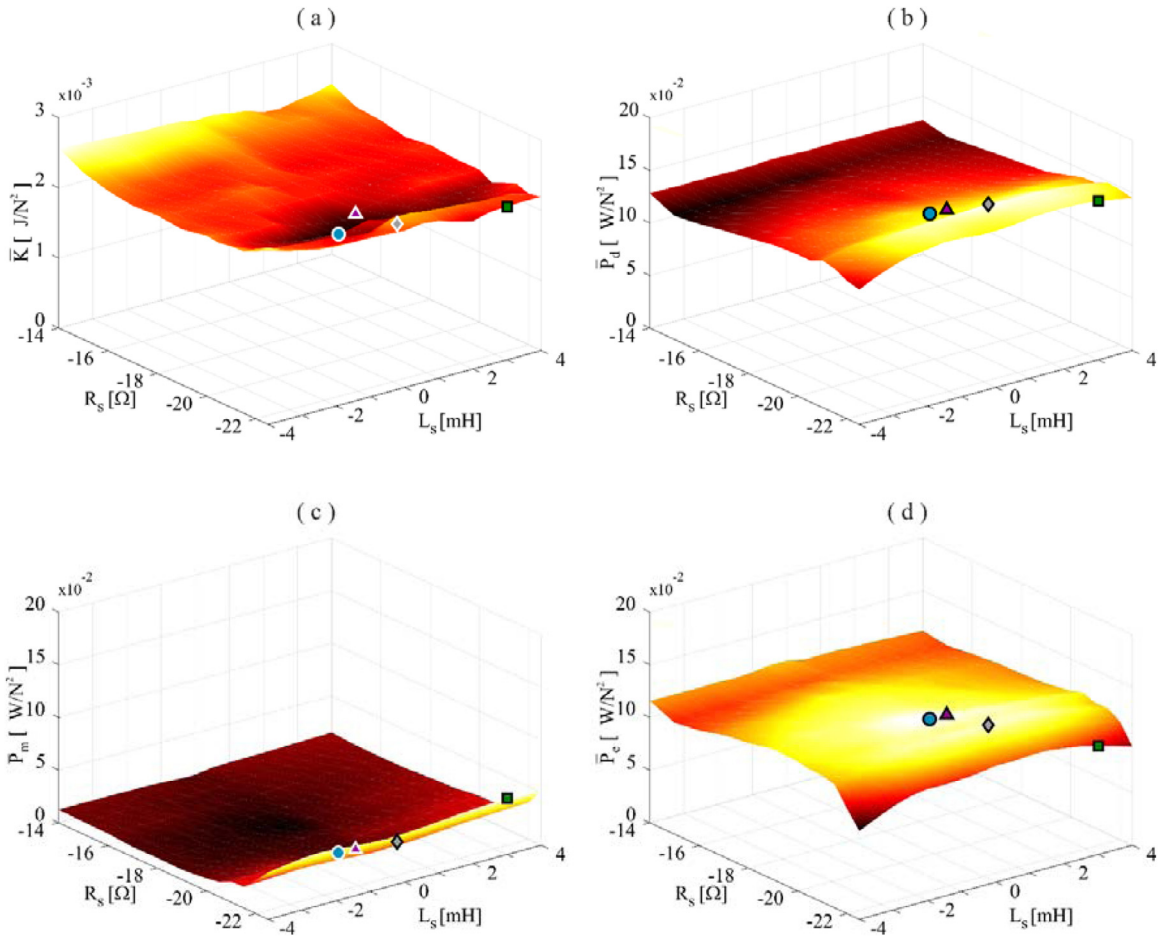

Fig. 11. Measured time-averaged total flexural kinetic energy of the plate (a), vibration power absorbed by the unit (b), mechanical power dissipated by the transducer (c) and electrical power dissipated by the shunt (d) with respect to the shunt resistance and inductance for the control of the third flexural mode. Cyan circle: minimum of the kinetic energy, grey diamond: maximum of the power absorbed by the unit, green square: maximum of the mechanical power dissipated by the transducer and purple triangle: maximum of the electric power dissipated by the coil and shunt.

Table 4
Optimal values of the shunt elements for the minimisation/maximisation of the four energy/power time-averaged functions considered in the experimental study.

Target mode	Natural frequency ω_r [Hz]	Integration bound $\Delta\omega_r$ [Hz]	$\arg\min \bar{K}$		$\arg\max \overline{P_a}$		$\arg\max \overline{P_m}$		$\arg\max \overline{P_e}$	
			R_s [Ω]	L_s [mH]	R_s [Ω]	L_s [mH]	R_s [Ω]	L_s [mH]	R_s [Ω]	L_s [mH]
Mode 1	46	40	-20.5	40	-22.0	45	-22.5	55	-15	10
Mode 3	112	40	-20.5	-0.5	-21.5	0.5	-22.5	3	-20.5	0

the transducer and time-averaged electrical power dissipated by the coil and shunt are in this case characterised by inverse bell-like shape and bell-like shape surfaces respectively. The map (c) has a global maximum marked by the green square at $R_s = -22.5$ Ω and $L_s = 3$ mH. The map (d) has instead a global maximum marked by the purple triangle at $R_s = -20.5$ Ω and $L_s = -1.5$ mH. As indicated by the cyan circle and grey diamond in this map, these values of the shunt inductance and resistance are closely located to the optimal values obtained in map (a) for the minimisation of the time-averaged flexural kinetic energy and in map (b) for the maximisation of the time-averaged vibration power absorbed by the unit. Therefore, as highlighted by the cyan circle, grey diamond and purple triangle in map (a), about the same reduction of the time-averaged flexural kinetic energy is produced regardless the shunt resistance and inductance are tuned to either minimise the time-averaged flexural kinetic energy or to maximise the time-averaged vibration power absorbed by the unit or to maximise the time-averaged electric power dissipated by the coil and shunt. Therefore, besides the time-averaged vibration power absorbed by the unit, the time-averaged electric power dissipated by the coil and shunt can equally be used to tune the shunt resistance and inductance in such a way as the unit minimises the time-average total flexural kinetic energy of the hosting

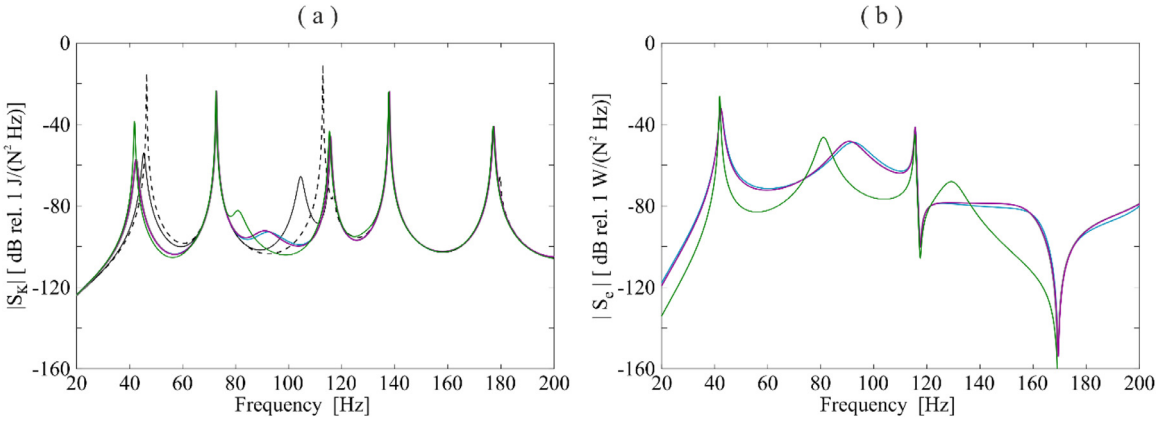

Fig. 12. Simulated spectra of the kinetic energy (a) and electrical power dissipated (b) PSDs for the plain plate (dashed black line) and the plate equipped with the unit in open circuit (solid thin black line) and shunted with optimal values for the minimisation of the time-averaged flexural kinetic energy (cyan lines) and the maximisation of the: time-averaged vibration power absorbed by the unit (grey lines), time-averaged mechanical power dissipated by the transducer (green lines) and time-averaged electrical power dissipated by the coil and shunt (purple lines) when the unit is tuned to control the resonant response of the third flexural mode.

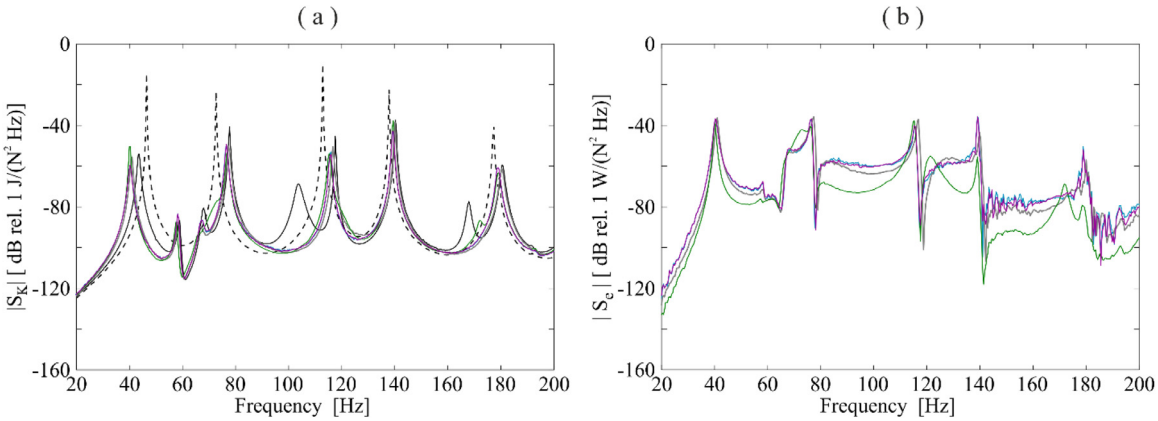

Fig. 13. Measured spectra of the kinetic energy (a) and electrical power dissipated (b) PSDs for the plain plate (dashed black line) and the plate equipped with the unit in open circuit (solid thin black line) and shunted with optimal values for the minimisation of the time-averaged flexural kinetic energy (cyan lines) and the maximisation of the: time-averaged vibration power absorbed by the unit (grey lines), time-averaged mechanical power dissipated by the transducer (green lines) and time-averaged electrical power dissipated by the coil and shunt (purple lines) when the unit is tuned to control the resonant response of the third flexural mode.

plate. In fact, the cyan, grey and purple lines in Figs. 12(a) and13(a) show that the spectrum of the time-average total flexural kinetic energy is equally reduced at the third resonance frequency when the resistance and inductance of the unit are set to either minimise the time-average total flexural kinetic energy of the plate or to maximise the time-averaged vibration power absorbed by the unit or to maximise the time-averaged electrical power dissipated by the coil and shunt components. Indeed, in this case, as shown in Figs. 12(b) and 13(b), at the third resonance frequency, the simulated and measured spectra of the electric power dissipated by the shunt is about the same when the shunt resistance and inductance are set to either minimise the time-averaged flexural kinetic energy or to maximise the time-averaged vibration power absorbed by the unit or to maximise the time-averaged electrical power dissipated by the coil and shunt.

5. Conclusions

This paper has investigated with simulations and experiments a local approach for the on-line tuning of a semi-active vibration control unit formed by an electromagnetic seismic transducer connected to a resistive-inductive shunt, which is mounted on a model wall structure subject to a white noise stochastic excitation. Firstly, the paper has demonstrated that, in general, the unit can be suitably tuned to control the resonant response of a target flexural mode of the plate by maximising the time-averaged vibration power absorbed by the unit in a finite frequency band around the resonance frequency of the target mode. This is quite an important outcome since it suggests a local tuning strategy based on the measurement of vibration power at the footprint of the unit, which, in contrast to the classical tuning laws based on the overall flexural response of the hosting structure, can be simply measured with a force cell and accelerometer or an impedance head.

Secondly, the paper has shown that, the unit can be duly tuned to control the resonant response of a target flexural mode of the plate by maximising the time-averaged electrical power dissipated by the coil and shunt components in a finite frequency band around the resonance frequency of the target mode. Indeed, apart the fundamental flexural mode, where the tuning generates a slightly lower vibration control effect, the unit produces nearly identical vibration control effects than the optimal approach based on the minimisation of the resonant response of the target flexural mode. This is even a more important outcome since it indicates that unit can be locally tuned by simply measuring the electrical power dissipated by the coil and the shunt components. This is quite a simple task, which does not require ad hoc sensors since it can be retrieved and processed directly in the adaptive shunt circuit. Hence, compact and lightweight semi-active control units can be developed and used in batches to control flexural vibration and sound radiation of thin walled structures at low audio frequencies.

Declaration of Competing Interest

The authors declare that they have no known competing financial interests or personal relationships that could have appeared to influence the work reported in this paper.

CRediT authorship contribution statement

Paolo Gardonio: Conceptualization, Data curation, Formal analysis, Investigation, Methodology, Visualization, Writing - review & editing. **Emanuele Turco:** Conceptualization, Data curation, Formal analysis, Investigation, Methodology, Visualization, Writing - review & editing. **Aleksander Kras:** Conceptualization, Data curation, Formal analysis, Investigation, Methodology, Visualization, Writing - review & editing. **Loris Dal Bo:** Conceptualization, Data curation, Formal analysis, Investigation, Methodology, Visualization, Writing - review & editing. **Daniel Casagrande:** Conceptualization, Data curation, Formal analysis, Investigation, Methodology, Visualization, Writing - review & editing.

Acknowledgements

The authors would like to acknowledge the DEVISU project which was supported by the Ministero dell'Istruzione, dell'Università e della Ricerca research funding programme PRIN 2017 and the Programma operativo del Fondo sociale europeo 2014/2020 della Regione Friuli Venezia Giulia - Progetto "HEaD HIGHER EDUCATION AND DEVELOPMENT" OPERAZIONE 1 UNIUD (FP1619942002, canale di finanziamento 1420AFPL01) .

References

[1] D.J. Thompson, J. Dixon, Vehicle noise, in: F. Fahy, J. Walker (Eds.), Advanced Applications in Acoustics, Noise and Vibration, Spon Press, London, 2004 Chapter 6.
[2] D.J. Thompson, Railway Noise and Vibration: Mechanisms, Modelling and Means of Control, Elsevier, Amsterdam, 2009.
[3] J.S. Mixon, J.F. Wilby, Interior Noise, in: H. H. Hubbard (Ed.), Aeroacoustics of Flight Vehicles: Theory and Practice. Volume 2: Noise Control. NASA Reference Publications, Hampton Virginia, 1991, Chapter 16.
[4] M.J. Brennan, N.S. Ferguson, Vibration control, in: F. Fahy, J. Walker (Eds.), Advanced Applications in Acoustics, Noise and Vibration, Spon Press, London, 2004 Chapter 12.
[5] D. Thompson, Noise Control, in: F. Fahy, D. Thompson (Eds.), Fundamentals of Sound and Vibration., CRC Press, Chichester, 2015, Chapter 5.
[6] R.S. Langley, F.J. Fahy, High frequency structural vibration, in: F. Fahy, J. Walker (Eds.), Advanced Applications in Acoustics, Noise and Vibration, Spon Press, London, 2004 Chapter 11..
[7] J.P. Den Hartog, Mechanical Vibrations, fourth ed., McGraw-Hill, New York, 1986.
[8] P. Gardonio, E. Turco, Tuning of vibration absorbers and Helmholtz resonators based on modal density/overlap parameters of distributed mechanical and acoustic systems, J. Sound Vib. 451 (2019) 32–70, doi:10.1016/j.jsv.2019.03.015.
[9] M. Zilletti, S.J. Elliott, E. Rustighi, Optimisation of dynamic vibration absorbers to minimise kinetic energy and maximise internal power dissipation, J. Sound Vib. 331 (2012) 4093–4100, doi:10.1016/j.jsv.2012.04.023.
[10] O. Nishihara, T. Asami, Closed-form solutions to the exact optimizations of dynamic vibration absorbers (minimizations of the maximum amplitude magnification factors), J. Vib. Acoust. 124 (2002) 576–582, doi:10.1115/1.1500335.
[11] S.H. Crandall, W.D. Mark, Random Vibration in Mechanical Systems, Academic Press, London, 1963.
[12] A.J. McDaid, B.R. Mace, A self-tuning electromagnetic vibration absorber with adaptive shunt electronics, Smart Mater. Struct. 22 (2013) 105013, doi:10.1088/0964-1726/22/10/105013.
[13] E. Turco, P. Gardonio, Sweeping shunted electro-magnetic tuneable vibration absorber: design and implementaion, J. Sound Vib. 407 (2017) 82–105, doi:10.1016/j.jsv.2017.06.035.
[14] S. Camperi, M. Ghandchi Tehrani, S.J. Elliott, Local tuning and power requirements of a multi-input multi-output decentralised velocity feedback with inertial actuators, Mech. Syst. Signal Process. 117 (2019) 689–708.
[15] M.A. Franchek, M.W. Ryan, R.J. Bernhard, Adaptive passive vibration control, J. Sound Vib. 189 (1996) 565–585, doi:10.1006/jsvi.1996.0037.
[16] K. Williams, G. Chiu, R. Bernhard, Adaptive-passive absorbers using shape-memory alloys, J. Sound Vib. 249 (2002) 835–848, doi:10.1006/jsvi.2000.3496.
[17] E. Rustighi, M.J. Brennan, B.R. Mace, A shape memory alloy adaptive tuned vibration absorber: design and implementation, Smart Mater. Struct. 14 (2005) 19–28, doi:10.1088/0964-1726/14/1/002.
[18] F. Weber, C. Boston, M. Maślanka, An adaptive tuned mass damper based on the emulation of positive and negative stiffness with an MR damper, Smart Mater. Struct. 20 (2010) 015012, doi:10.1088/0964-1726/20/1/015012.
[19] P. Gardonio, D. Casagrande, Shunted piezoelectric patch vibration absorber on two-dimensional thin structures: tuning considerations, J. Sound Vib. 395 (2017) 26–47, doi:10.1016/j.jsv.2017.02.019.
[20] N. Alujević, I. Tomac, P. Gardonio, Tuneable vibration absorber using acceleration and displacement feedback, J. Sound Vib. 331 (2012) 2713–2728, doi:10.1016/j.jsv.2012.01.012.

[21] G. Zhao, N. Alujević, B. Depraetere, P. Sas, Dynamic analysis and H2 optimisation of a piezo-based tuned vibration absorber, J. Intell. Mater. Syst. Struct. 26 (2015) 1995–2010, doi:10.1177/1045389X14546652.
[22] C. Paulitsch, P. Gardonio, S.J. Elliott, Active vibration damping using an inertial, electrodynamic actuator, J. Vib. Acoust. 129 (2007) 39–47, doi:10.1115/1.2349537.
[23] A.J. Fleming, S.O.R Moheimani, Inertial vibration control using a shunted electromagnetic transducer, IEEE/ASME T. Mech. 11 (2006) 84–92, doi:10.1109/TMECH.2005.863364.
[24] B. Yan, X. Zhang, Y. Luo, Z. Zhang, S. Xie, Y. Zhang, Negative impedance shunted electromagnetic absorber for broadband absorbing: experimental investigation, Smart Mater. Struct. 23 (2014) 125044, doi:10.1088/0964-1726/23/12/125044.
[25] X. Zhang, H. Niu, B. Yan, A novel multimode negative inductance negative resistance shunted electromagnetic damping and its application on a cantilever plate, J. Sound Vib. 331 (2012) 2257–2271, doi:10.1016/j.jsv.2011.12.028.
[26] E. Turco, P. Gardonio, R. Petrella, L. Dal Bo, Modular vibration control unit formed by an electromagnetic proof-mass transducer and sweeping RL-shunt, J. Vib. Acoust. 142 (2020) 0610005-1-16, doi:10.1115/1.4047068.
[27] D.B. Hiemstra, G. Parmar, S. Awtar, Performance tradeoffs posed by moving magnet actuators in flexure-based nanopositioning, IEEE/ASME T. Mech. 19 (2014) 201–212, doi:10.1109/TMECH.2012.2226738.
[28] L. Dal Bo, P. Gardonio, Energy harvesting with electromagnetic and piezoelectric seismic transducers: unified theory and experimental validation, J. Sound Vib. 433 (2018) 385–424, doi:10.1016/j.jsv.2018.06.034.
[29] H.A. Sodano, J.-S. Bae, D.J. Inman, W.Keith Belvin, Concept and model of eddy current damper for vibration suppression of a beam, J. Sound Vib. 288 (2005) 1177–1196, doi:10.1016/j.jsv.2005.01.016.
[30] J.-S. Bae1, J.-H. Hwang, J.-S. Park, D.-G. Kwag, Modeling and experiments on eddy current damping caused by a permanent magnet in a conductive tube, J. Mech. Sci. Technol. 23 (2009) 3024–3035, doi:10.1007/s12206-009-0819-0.
[31] J. Vanderkooy, A model of loudspeaker driver impedance incorporating eddy currents in the pole structure, J. Audio Eng. Soc. 37 (1989) 119–128.
[32] W. Marshall Leach, Loudspeaker voice-coil inductance losses: circuit models, parameter estimation, and effect on frequency response, J. Audio Eng. Soc. 50 (2002) 442–450.
[33] P. Gardonio, S. Miani, F. Blanchini, D. Casagrande, S.J. Elliott, Plate with decentralised velocity feedback loops: power absorption and kinetic energy considerations, J. Sound Vib. 331 (2012) 1722–1741, doi:10.1016/j.jsv.2011.12.013.
[34] J.S. Bendat, A.G. Piersol, Random Data Analysis and Measurement Procedure, Wiley & Sons, Chichester, 1990.
[35] R.W. Clough, J. Penzien, Dynamics of Structures, McGraw-Hill, NewYork, 1975.
[36] R.S. Langley, Can an undamped oscillator dissipate energy? J. Sound Vib. 206 (1997) 624–626, doi:10.1006/jsvi.1997.1066.
[37] R.S. Langley, A general mass law for broadband energy harvesting, J. Sound Vib. 333 (2014) 927–936, doi:10.1016/j.jsv.2013.09.036.
[38] E. Halvorsen, Energy harvesters driven by broad band random vibrations, J. Microelectromech. Syst. 17 (2008) 1061–1071, doi:10.1109/JMEMS.2008.928709.
[39] J.T. Scruggs, An optimal stochastic control theory for distributed energy harvesting networks, J. Sound Vib. 320 (2009) 707–725, doi:10.1016/j.jsv.2008.09.001.
[40] W. Soedel, Vibration of Shells and Plates, 3rd edition, CNR Press, New York, 2004.
[41] L. Meirovitch, Principles and Techniques of Vibration, Prentice Hall, Upper Saddle River, NJ, 1997.
[42] G.B. Warburton, The vibration of rectangular plates, Proc. Inst. Mech. Eng. 168 (1954) 371–384.